Electrical conductivity images of Quaternary faults and Tertiary detachments in the California Basin and Range

Stephen K. Park

Institute of Geophysics and Planetary Physics, University of California, Riverside, California, USA

Brian Wernicke

Division of Geological and Planetary Sciences, California Institute of Technology, Pasadena, California, USA

Received 4 September 2001; revised 4 August 2002; accepted 27 August 2002; published XX Month 2003.

[1] Comparison of an electrical resistivity section derived from magnetotelluric (MT) data to a geologic section extending eastward from the Sierra Nevada near latitude 36°20′N shows that the crust is dominated by steeply dipping conductive features that correlate with active strike-slip faults. While there is a subhorizontal conductor at a depth ~20 km beneath some of the profile, it is broken by vertical structures associated with the active strike-slip faults. The continuous subhorizontal anomalies in the lower crust typically observed in extensional regions are therefore absent in the resistivity section. The present-day strike-slip tectonic regime as indicated by geodetic data in this part of the Basin and Range is not producing features that could be inferred to indicate subhorizontal shear zones resulting from lateral crustal flow during extension. Because the Miocene tectonic regime resulted in the formation of metamorphic core complexes and thus was accompanied by such flow, the present regime appears to represent a fundamental transition in the mode of crustal deformation in the region. A serendipitous result of our study was the identification on resistivity sections of carbonate aquifers in the upper crust. Comparison of resistivities from the MT section to measured fluid resistivities from springs and boreholes suggests that the aquifers must be heterogeneous, with more saline brines occupying the deepest portions of the carbonates. *INDEX TERMS:* 8109 Tectonophysics: Continental tectonics—extensional (0905); 8010 Structural Geology: Fractures and faults; 8045 Structural Geology: Role of fluids; 5109 Physical Properties of Rocks: Magnetic and electrical properties; *KEYWORDS:* magnetotellurics, Basin and Range, Death Valley, detachment faults. **Citation:** Park, S. K., and B. Wernicke, Electrical conductivity images of Quaternary faults and Tertiary detachments in the California Basin and Range, *Tectonics*, *22*(0), XXXX, doi:10.1029/2001TC001324, 2003.

0278-7407/03/2001TC001324$12.00

1. Introduction

[2] The Basin and Range province of eastern California (Figure 1) is a prime natural laboratory for studying the causes and consequences of large-magnitude intracontinental deformation. The region was markedly deformed as the Sierra Nevada block moved some 250 km west-northwestward away from the Colorado Plateau since 16 Ma [*Wernicke and Snow*, 1998]. This motion was predominantly due west until 8 to 10 Ma, when there was a shift to a NNW motion that has persisted to the present. Post-8 Ma motion has proceeded at rates of 10 to 15 mm/yr. The intervening Basin and Range ultimately developed into a patchwork of relatively undeformed crustal blocks separated by regions strongly deformed by extension, strike-slip and shortening, with an overall east-west constrictional strain field [*Wernicke et al.*, 1988; *Mancktelow and Pavlis*, 1994]. Quantitative reconstruction of the strain pattern suggests that in regions of large-magnitude extension such as Death Valley and environs, the upper 12–15 km of the crust have been almost completely removed [*Snow and Wernicke*, 2000]. Active deformation as revealed by space-geodetic measurements is predominantly right-lateral simple shear oriented N20°W, at about 9 mm/yr, somewhat slower than the post-8 Ma average deformation rate [*Bennett et al.*, 1999, 2003].

[3] The outstanding issues raised by this history include the hypothesis that removal of the upper crust over large areas in the Basin and Range was compensated by eastward flow of deep crust from beneath the Sierra Nevada [e.g., *Wernicke*, 1992] because the crustal thicknesses of unextended areas such as the Sierra Nevada and Inyo Mountains are roughly the same as that of the highly extended Death Valley region [*Wernicke et al.*, 1996; *Fliedner et al.*, 1996; *Jones and Phinney*, 1998]. Further, controversy remains as to whether the strain pattern in the region results mainly from right-lateral strike-slip faulting or crustal extension. Some authors have suggested that the present-day pattern of right-lateral shear is representative of the entire deformational history of the region [e.g., *Serpa and Pavlis*, 1996]. Others have suggested a transition occurred in late Miocene time from a predominantly extensional strain field, with its attendant lateral flow exposing metamorphic core complexes [e.g., *Holm and Dokka*, 1993; *Hoisch and Simpson*, 1993; *Hoisch et al.*, 1997], to the strike-slip one that dominates today [e.g., *Snow and Wernicke*, 2000].

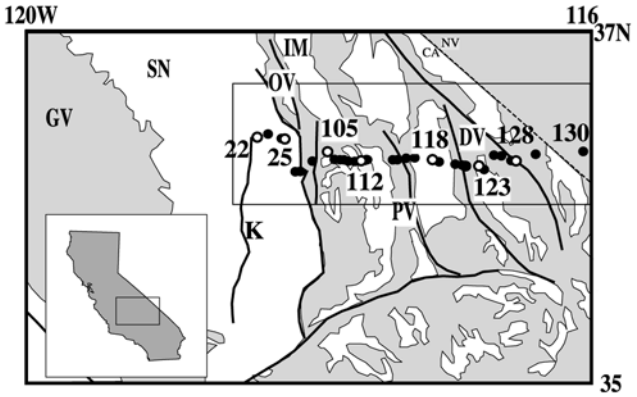

Figure 1. Map showing locations of MT stations (black for broadband and white dots for long period sites) superimposed on distribution of major mountain ranges (shaded) and alluvial valleys (unshaded), and location of Figure 2 (box surrounding MT stations). Inset shows location of Figure 1 in California. MT sites denoted with white dots are keyed to site labels in later figures. Symbols used are: DV, Death Valley; GV, Great Valley; K, Kern River fault; IM, Inyo Mountains; OV, Owens Valley; PV, Panamint Valley; and SN, Sierra Nevada.

[4] To evaluate the active tectonic framework at crustal scales, a magnetotelluric (MT) transect was completed in 1993 and augmented in 1997. Active structures in the crust are often conduits for fluids. One of the most sensitive indicators of these fluids is electrical conductivity, which depends on porosity, and the salinity and interconnectivity of the fluid [e.g., *Jones*, 1992]. Our goal was to image zones of anomalously high conductivity and compare these to the two competing tectonic hypotheses. In particular, could the observed Miocene subhorizontal mylonite zones have developed in a strike-slip regime as suggested by *Serpa and Pavlis* [1996]? If so, then the MT profile would show subhorizontal conductors beneath the region which would be suggestive of lateral flow. Alternatively, if an older Miocene extensional province was overprinted by the present strike-slip regime as suggested by *Snow and Wernicke* [2000], then the MT profile would show a predominance of vertically oriented conductive zones.

[5] Vertical conductive zones characterize active strike-slip faults elsewhere. For example, high conductivities (10–100 times more conductive than surrounding upper crust) are observed along the San Andreas fault zone and are attributed to fluids [*Mackie et al.*, 1997; *Unsworth et al.*, 1997]. Although some types of mineralization (i.e., graphite precipitation) can lead to conductive old and inactive faults, active deformation is generally required to maintain the interconnectivity of the pore space and therefore high conductivity that is otherwise lost to mineral precipitation in the absence of tectonism. This pore space interconnectivity contributes to the high conductivities seen along faults as modeled above. In regimes dominated by crystal-plastic deformation, laboratory experiments also show that minerals are preferentially wetted by fluids while they are actively deforming, but are not wetted once the deformation ceases [*Watson and Lupulescu*, 1993; *Tullis et al.*, 1996]. This enhanced fluid connectivity further increases the electrical conductivity of such regions, but only during active deformation.

[6] Extensional regimes are generally characterized by the development of subhorizontal tectonic elements such as low-angle normal faults and detachments, mylonite zones, deep crustal lateral flow, and subhorizontal conductors. Where extension is active, as in the Rio Grande rift and across the eastern half of the northern Basin and Range, the deep crust is characterized by a laterally persistent, subhorizontal layer of high conductivity [*Jiracek et al.*, 1987; *Wannamaker et al.*, 1997]. Electrical conductivities in deep crustal regions where lateral flow is presumed to be active are approximately 10 times larger than in the surrounding crust.

[7] Our MT profile shows a predominance of vertically oriented conductors versus subhorizontal ones, suggesting that the current strike-slip tectonic regime produces only vertical features. We will present first the results of the MT transect from the Sierra Nevada to Death Valley Junction (Figure 1) and discuss how the resulting conductivity image was created. We then compare the MT section to a geologic cross section based on surface geology to evaluate any correspondence between the distribution of active structures and zones of high conductivity. An unexpected result of this study is that the MT section imaged a number of good conductors in the uppermost crust away from any active structures that appear to correspond to carbonate aquifers.

2. Tectonic Setting

[8] The principal active tectonic elements in the region include three major zones of right-lateral shear, including, from east to west, the Death Valley (NFZ and CFZ), Panamint Valley (PVF), and Owens Valley (OVF) fault zones (Figure 2). The Death Valley and Panamint Valley fault zones are considered the type examples of extensional "pull apart" fault systems [*Burchfiel and Stewart*, 1966], with northwest striking segments exhibiting pure strike-slip and north striking segments exhibiting a component of normal motion, which is responsible for the formation of the modern alluvial valleys. The section crosses the southernmost extent of the 1872 rupture on the Owens Valley fault zone [*Beanland and Clark*, 1994]. In Owens Valley, the section also crosses a prominent northeast trending scarp on the northwestern piedmont of the Coso Range, interpreted as a northwest dipping Quaternary normal fault by *Streitz and Stinson* [1974] but regarded as only a wave-cut terrace by *Beanland and Clark* [1994] (queried fault on Figure 2). Other strike-slip fault zones, including the northwest striking Furnace Creek (FC) and Stewart Valley (SV) faults, may have been recently active but unlike the other three major fault systems, they do not display throughgoing late Quaternary breaks [e.g., *Schweickert and Lahren*, 1997].

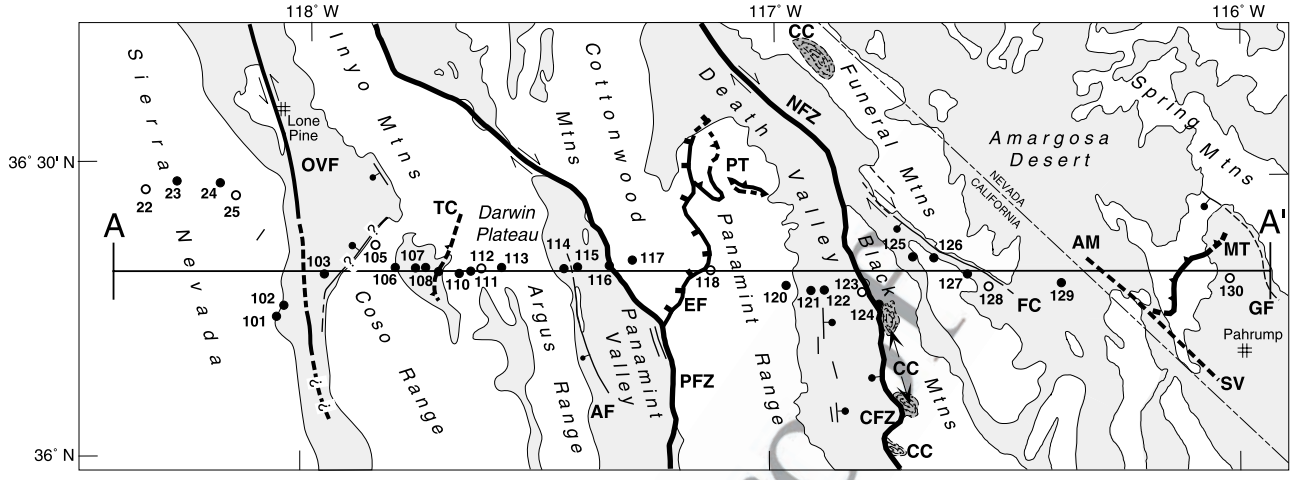

Figure 2. Map showing location of line of geologic section A–A′ in Figure 3a and locations of MT sites (dots with numbers) with respect to selected geological features. Shaded areas are modern alluvial valleys. Thick sinuous lines show traces of faults, including Cenozoic high-angle normal faults (bar and ball on downthrown side), low-angle normal faults (tick marks), and strike-slip faults (arrows show sense of motion). Pre-Cenozoic thrust faults shown with teeth. Faults are dashed where trace is concealed beneath younger deposits or approximately located and are queried where existence is equivocal. Fault abbreviations, from west to east: OVF, Owens Valley fault zone; TC, Talc City thrust; AF, Ash Hill fault; PFZ, Panamint Valley fault zone; EF, Emigrant fault; PT, Panamint thrust; NFZ, Northern Death Valley fault zone; CFZ, central Death Valley fault zone; FC, Furnace Creek fault zone; SV, Stewart Valley/ Pahrump Valley fault zone; MT, Montgomery thrust; GF, Grapevine fault. Other abbreviations: CC, exposures of core complex mylonites; AM, Ash Meadows area.

[9] These structures are superimposed on four main pre-Quaternary tectonic elements, including (1) the Mesozoic Sierra Nevada batholith; (2) the Cordilleran miogeoclinal wedge, which comprises a more or less conformable package of west thickening Neoproterozoic through early Mesozoic sedimentary rocks about 10 km thick; (3) a system of east vergent pre-Cenozoic thrust faults that telescoped the sedimentary wedge from late Paleozoic to Cretaceous time; and (4) a system of predominantly east dipping normal faults and associated basins, developed mainly in Miocene time.

[10] We constructed a geologic cross section along the line of the MT transect (Figure 3a; see Appendix A for details). In general, the upper ~5 km of the section are constrained by published geologic mapping, taking advantage of the fact that the miogeoclinal section is thick and conformable, and so in some areas sedimentary units can be extrapolated to significant depth with reasonable confidence. In addition to the geologic constraints, Figure 3a shows downward projections to mid-crustal depths of the three major active fault zones on the basis of the MT data, as elaborated below. It also includes the position of the Moho (M), a lower crustal positive velocity anomaly (LCP) and a mid-crustal negative velocity anomaly (MCN) determined from analysis of teleseismic data [*Jones and Phinney*, 1998; R. A. Phinney, oral communication, 2001].

[11] Batholithic rocks occupy the western quarter of the transect, and are mainly Jurassic and Cretaceous granodiorites and quartz monzonites (cross section units Jgd, Kgd, and Jqm), except for a small body of Cretaceous muscovite granite (Kg) in the Panamint Range. The remainder of the section is underlain primarily by Proterozoic basement (XYb) and unconformably overlying stratified units. Pre-Tertiary strata include the Pahrump Group (Zp) and unconformably overlying miogeosynclinal strata whose lower part is predominantly clastics (ZCc) and upper part mainly carbonates (CM, PTr). Unit CM is a major aquifer in the southern Great Basin region, and thus its geometry is an important element in interpreting the shallow crustal conductivity structure [*Winograd and Thordarson*, 1968, 1975]. Unconformably overlying Tertiary units are divisible into lower, middle and upper Miocene strata (lM, mM, and uM, respectively), Pliocene non-volcanic (P) and volcanic strata (Pb), and Pliocene to Quaternary fill of the modern valleys (PQ).

[12] Major pre-Quaternary structures crossed by the section include three significant pre-Cenozoic thrust faults, the Montgomery (MT), Panamint (PT) and Talc City (TC) thrusts, all east vergent. Large-displacement normal fault systems serve to tectonically denude the upper crust from most of the eastern half of the section, and are well exposed in the Funeral Mountains, Black Mountains and Panamint Range. These fault systems appear to have been active in succession from east to west [e.g., *Snow and Wernicke*, 2000], beginning with faults in the Amargosa Desert and Funeral Mountains areas from 14 to 10 Ma (detachment with one tick mark on the section), faults active from 10 to 6 Ma (detachment with two tick marks) and finally faults active

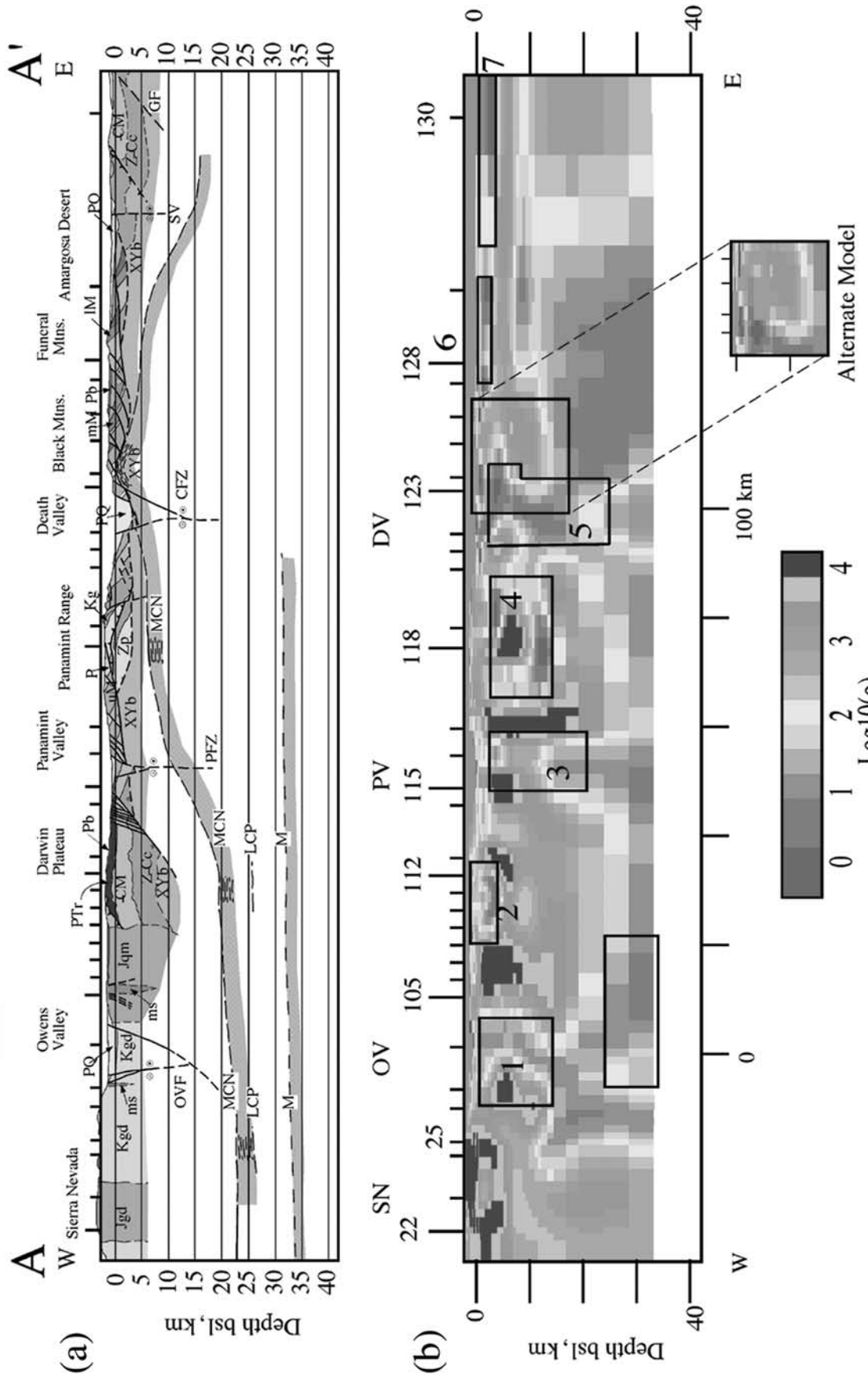
A
A'
W
E
Sierra Nevada
Owens Valley
Darwin Plateau
Panamint Valley
Panamint Range
Death Valley
Black Mtns.
Funeral Mtns.
Amargosa Desert
Jgd
Kgd
ms
Jqm
PTr
Pb
PQ
lM
mM
Kg
Zg
R
XYb
ZCc
CM
GF
SV
CFZ
PFZ
OVF
MCN
LCP
M
(a)
Depth bsl, km
SN
OV
PV
DV
W
E
100 km
(b)
Alternate Model
Log10(ρ)

mainly after 6 Ma, including the Emigrant fault system (EF, detachment with three tick marks on the section).

[13] Deep structural levels are brought to the surface throughout the strongly extended region, and extreme denudation has exposed domes of Tertiary mylonite that define core complexes in the Black Mountains and Funeral Mountains (CC) which are interpreted to represent mid-crustal lateral flow or shear at the onset of rifting [e.g., *Wernicke*, 1992]. As elaborated below, the upper boundary of the core complex mylonites mapped in the Black Mountains is a strong candidate for the MCN imaged teleseismically to the west beneath the Panamint Range, Darwin Plateau area and easternmost Sierra Nevada, and hence all four are depicted with the same patterning in Figure 3a, and are interpreted to be laterally continuous. As normal faulting and extension die out to the east, this same structural level must deepen eastward, we presume to mid-crustal depths, beneath the relatively unextended Spring Mountains block.

3. MT Method

[14] The MT method relies on recording natural variations of the Earth's electric and magnetic fields. The following summary is a distillation of 5 decades of work by many scientists in the MT field; good reviews are given by *Vozoff* [1991] or *Nabighian* [1991]. Small (1:50,000,000 of the Earth's total field) variations of the magnetic field induce electrical currents in the Earth. These currents are distorted and channeled by the Earth's heterogeneous conductivity structure. Horizontal components of the vector electric and magnetic field are recorded as time series at an MT site, and a period-dependent impedance tensor between the source magnetic field and the induced electric field is calculated. The tensor impedances are decomposed into two principal impedances (just as areal strain can be decomposed into two principal strains). These impedances, or modes, are generally orthogonal to one another and are usually parallel or perpendicular to geologic strike if the structure is 2-D. The mode perpendicular to the structure is called the transverse magnetic (TM) mode. It is sensitive primarily to changes in conductivity that cross the profile. The mode parallel to the structure is the transverse electric (TE) mode. This mode responds primarily to conductive bodies with the same strike as the geologic structure, but truncations of these bodies off the profile can have a profound effect on the data. The TE mode is thus more affected by 3-D structure than is the TM mode [*Wannamaker*, 1999].

[15] The vertical magnetic field is also recorded at MT sites, and a transfer function relates the vertical to the horizontal magnetic fields. This transfer function is sensitive to the distribution of 2-D conductors in the Earth, similar to the TE mode [*Schmucker*, 1970]. These transfer functions are often represented as induction vectors which show the direction of the greatest correlation between the vertical and horizontal magnetic fields. We normally plot the real components of the induction vectors, which usually point towards 2-D conductors [*Schmucker*, 1970].

[16] Magnitudes and phases of each principal impedance mode vary with period. The magnitude is converted to an apparent resistivity that is equal to the true resistivity only when the earth is homogeneous [*Vozoff*, 1991]. Otherwise, the apparent resistivity is transformed to true resistivity (which is the inverse of conductivity) through a process called inversion. Because the MT fields are dissipative waves in the earth, they attenuate with depth. The depth of penetration depends nonlinearly on the conductivity of the earth and the period of the fields. Longer periods penetrate deeply and/or distantly, while shorter periods decay more rapidly and penetrate only the shallower and/or closer structure. Because of the nonlinearity in the depth of penetration, simple conversion from period to depth is unreliable. Inversion is used to match simulated responses from conductivity sections to the observed data (just as migration is used to convert a seismic reflection time section to a depth section). The inversion process involves subdividing the Earth into blocks of constant resistivity and then solving for those resistivities [e.g., *de Groot-Hedlin and Constable*, 1990; *Smith and Booker*, 1991; *Rodi and Mackie*, 2001]. The MT inversion is fundamentally underdetermined because the number of blocks is larger than the

Figure 3. (opposite) (a) Geologic cross section across MT transect. XYb, Proterozoic crystalline basement; Zp, Pahrump Group; ZCc, Neoproterozoic-Cambrian clastic strata; CM, Cambrian to Mississippian carbonate strata (lower carbonate aquifer), PTr, upper Paleozoic and Triassic strata; ms, metasedimentary screens within Mesozoic plutons; Jqm, Jurassic quartz monzonite; Jgd, Jurassic granodiorite; Kgd, Cretaceous granodiorite; lM, mM and uM, lower, middle and upper Miocene rift basin deposits and intercalated volcanics; P, Pliocene rift deposits; Pb, Pliocene volcanics, mainly basalt; PQ, Pliocene and Quaternary alluvial fill of modern valleys. Dot and cross symbols indicate motion along faults toward and away from reader, respectively. Thrust faults shown with teeth, major detachments with one, two or three tick marks, in order of decreasing age. Tick marks along the top of the section show positions of MT sites. Seismic interfaces from *Jones and Phinney* [1998] shown with heavy dot-dash lines where observed from arrays in the Sierra Nevada, Darwin Plateau and Panamint Range (the latter from R.A. Phinney, oral communication, 2001), interpolations and extrapolations shown with thinner lines and shading. MCN, mid-crustal negative; LCP, lower crustal positive; M, Moho. Fine dashes, Tertiary mylonite zones discussed in text. (b) Preferred MT resistivity cross sections from 2-D inversion. Regions outlined for sensitivity testing (black boxes) are numbered 1–7. See text for results of testing. The MT model is truncated at the base of the crust for comparison to Figure 3a. Inset on MT section shows alternate model for Black Mountains which does not have a thick conductive region east of zone 5. Common logarithm of resistivity is plotted in section; see scale at bottom. This scale is used because of the wide range of values seen in this physical parameter. See captions of Figures 1 and 2 for explanation of symbols. See color version of this figure at back of this issue.

number of apparent resistivities and phases; this can lead to unnecessarily complex conductivity structure unless constraints are added to smooth the model [e.g., *de Groot-Hedlin and Constable*, 1990]. These constraints eliminate much, but not all, of the spurious structure and leave behind more robust models. Testing the robustness of the remaining features that have been deemed geologically important is a routine component of interpretation; it may be possible to find an alternate model that fits the data as well as does the preferred model. Finding an alternate model usually consists of constraining resistivities in the region to be tested and then running the inversion again [*Park et al.*, 1996].

4. Magnetotelluric Soundings

[17] The E-W MT profile consisting of 33 broadband sites (black dots in Figure 1) and 7 long period sites (open circles in Figure 1) spanned ~200 km near latitude 36°20′N between the axis of the High Sierra Nevada to east of Death Valley. Note that this profile was part of a larger survey, the western component of which is interpreted by *Park et al.* [1996]. Two types of MT instrumentation were used in this study because data for the broadband sites were generally reliable for periods of 0.001–200 s only, and the long period instruments extended that range to 10,000 s. Details of the data acquisition and processing of the composite data set, on which the crustal section is based, are presented in Appendix B. Only the MT impedances from the broadband sites were used, while both the MT impedances and magnetic transfer functions from the long period sites were included in the modeling.

[18] The average N-S geoelectric strike derived from the MT impedances is subparallel to the regional geologic strike of N10W [*Jennings*, 1977] and matches the estimate of geoelectric strike from the magnetic induction vectors (Appendix B). Because of these similar strike directions and their consistency across the profile, we concluded that a 2-D cross section oriented E-W was appropriate for modeling.

[19] Pseudosections for the apparent resistivities and phases of the MT profile show patterns that are consistent to first order with the surface geology (Figure 4). High resistivities characterize the crystalline rocks of the Sierra Nevada, with decreasing values to the east. The intervening region between the Sierra Nevada and Death Valley is moderately resistive, with much lower values in the region of Death Valley and eastward (Figure 4). The Panamint block shows up as a somewhat isolated resistive region between sites 105–120 in the E-W apparent resistivity cross section (PV in Figure 4). Note that the N-S apparent resistivity and phase pseudosections do not include all of the data from suspect sites 101–115 (see Appendix B), so the corresponding image of the Panamint block in the N-S apparent resistivity section is less defined.

[20] Induction vectors were oriented generally E-W and magnitudes rarely exceeded 0.1–0.2 except where the data were noisy. The one exception was a vector magnitude of 0.7 at site 123, on the edge of Death Valley. Induction vectors are normally aligned perpendicular to structural strike with 2-D bodies, so our choice of a N-S geoelectrical strike is reasonable.

5. Two-Dimensional Modeling

[21] We modeled the MT data with a 2-D regularized inversion algorithm [*Rodi and Mackie*, 2001] that jointly minimizes the data misfit and the deviation of the final model from an a priori one. Only a subset of the model will be shown here; the actual model extended from 9000 km westward into the Pacific Ocean to 9000 km eastward and to a depth of 1000 km in order to achieve accurate finite difference computations. Because deviations from the a priori model are included in the minimization process, it is sometimes possible to bias the final result with the starting model. We therefore chose a simple a priori model consisting of a layered half space with the upper 90 km represented by a top layer 10 km thick (1000 ohm-m) and a lower layer 80 km thick (500 ohm-m). Any lateral variations in the final model are thus generated by the inversion to fit the data and are actually penalized by the model constraints.

[22] Only some of the data were used in the inversion. All of the E-W principal impedances and the E-W magnetic transfer functions (both real and imaginary components) were included in the inversion. For our model, this is the TM mode discussed above. The N-S principal impedances at sites 101–116 were excluded because of system problems (see Appendix B for discussion). For our model, the N-S mode is the TE mode discussed above. The N-S impedances from the remaining sites were included, but given lesser weights in the inversion because the TE mode is often affected by truncation of structure along strike (in this case, to the north or south of the profile) [*Wannamaker et al.*, 1984; *Wannamaker*, 1999]. Specific to our profile, *Mackie et al.* [1996] show that the N-S mode, but not the E-W mode, at a site in Panamint Valley is affected by regional 3-D structure including the Transverse Ranges adjacent to the Pacific Ocean. Thus we give lesser weight to the mode likely to be contaminated by regional 3-D effects.

[23] Data are weighted in the inversion by the inverse of their variances [*Rodi and Mackie*, 2001]. A data point with a low variance is given a very large weight. Formal errors from the time series analysis were often smaller than the scatter of the impedance estimates between adjacent peri-

Figure 4. (opposite) Pseudosections of MT data and associated fits to data from final model. Each section is labeled with the type of data (apparent resistivity or phase) and it orientation (N-S or E-W). Color scales for apparent resistivities and phases are shared, but ranges are labeled differently for these quantities. Similarly, scales for difference pseudosections for apparent resistivity and phase are shared but ranges are different. Sections of data excluded from the inversion are shown with black areas in difference pseudosections. Note that most of the TE mode (i.e., the N-S mode) was not used in the inversion. The difference pseudosections reveal no systematic misfits. See color version of this figure at back of this issue.

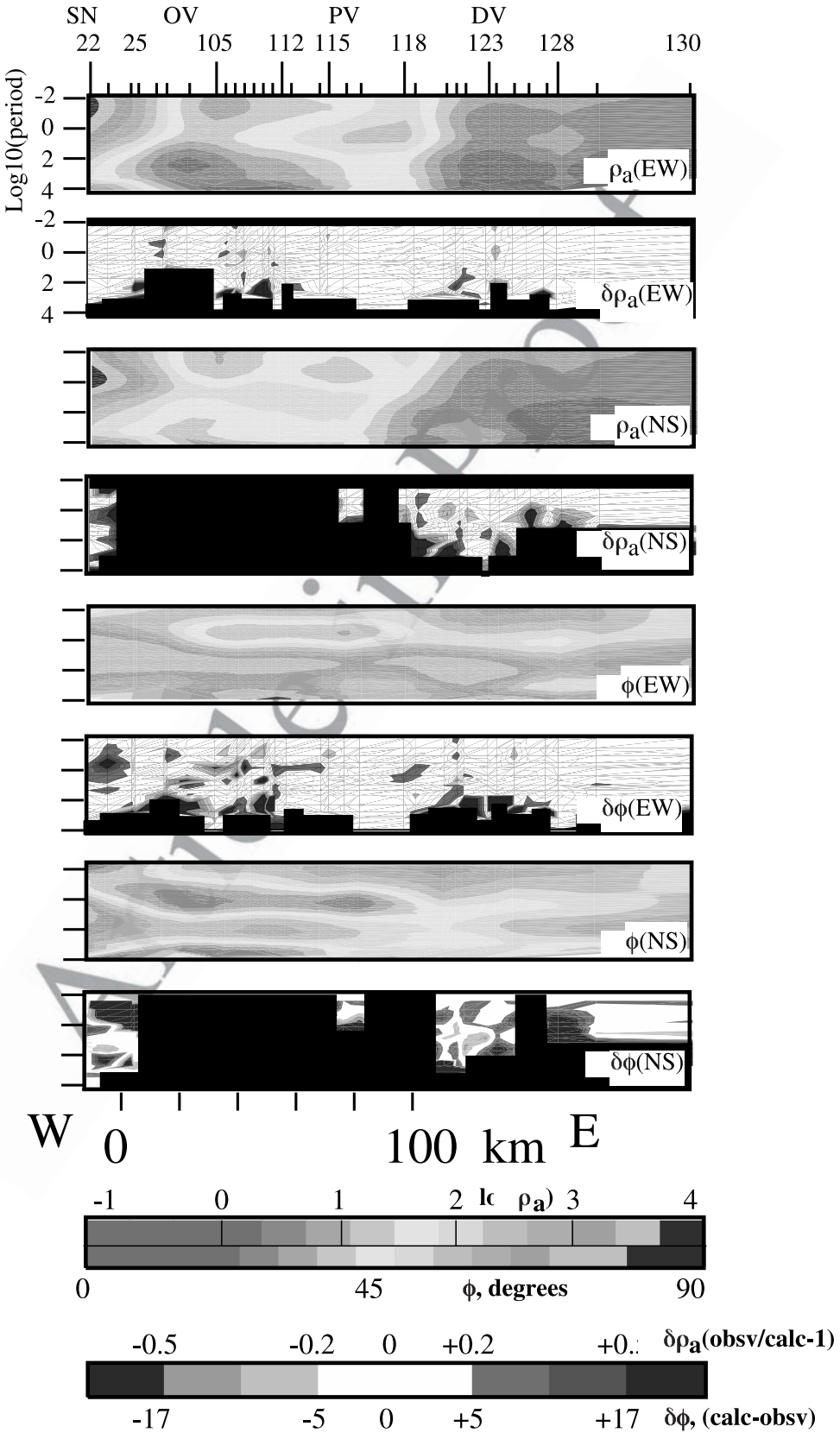
SN
OV
PV
DV
22
25
105
112
115
118
123
128
130
Log10(period)
-2
0
2
4
ρa(EW)
δρa(EW)
ρa(NS)
δρa(NS)
φ(EW)
δφ(EW)
φ(NS)
δφ(NS)
W
0
100 km
E
-1
0
1
2
lo ρa)
3
4
0
45
φ, degrees
90
-0.5
-0.2
0
+0.2
+0.
δρa(obsv/calc-1)
-17
-5
0
+5
+17
δφ, (calc-obsv)

ods. Error floors of 5% in N-S apparent resistivity and 0.05 radians (2.8°) in N-S phase were chosen based on this scatter. Use of this error floor as a minimum error for all points reduces the influence of data values with unrealistically low error estimates. Error floors for 20% for N-S apparent resistivity and 0.2 radians (11.2°) for the N-S phase reflected larger scatter in these data and the lesser weight given to these data. Finally, an error floor of 20% was chosen for the magnetic transfer functions based on the composite quality of the long period and the broadband data.

[24] After a series of trials to determine the optimal balance between fitting the data and deviating from the a priori model, the model resulting from over 250 iterations fit the data with an overall RMS error of 2.06 (misfit about twice the estimated errors in the data). Given the variable quality of the contractor data, this is a reasonable level of misfit. Comparison of the data to the fits predicted by the model show that there are generally low differences (Figure 4). Apparent resistivities and phases for the E-W principal impedance are fit to within 8° for the phases and 20% for the apparent resistivities, but the misfits for the N-S values are larger. This is expected because this mode is affected by changes in structure along strike. The sparseness of the points used for the N-S mode results from the poor data quality discussed earlier (Figure 4; Appendix B).

[25] The resistivity model in this region shows a generally resistive crust broken with 7 prominent conductive zones (Figure 3b). The model is truncated near seismic Moho because the focus of this paper is on the crustal structure. Zones 1, 3, and 5 extend to deep crustal levels and correspond to active faults in the Owens, Panamint, and Death Valleys (Figure 3b). Zones 2, 4, 6, and 7 do not extend into the deeper crust and do not correspond to identified active structures. Because the MT method is most sensitive to conductors, the absence of conductive material beneath zones 2, 4, 6, and 7 implies that they are truncated in the shallow crust.

[26] Because of the nonuniqueness in the inversion process, it is possible for artifacts to be introduced into the resistivity section. Specific regions of the model in Figure 3b are tested for robustness following the procedures outlined by *Park et al.* [1996]. The prominent conductor dipping westward beneath Owens Valley (zone 1) is needed to depths of at least 17 km bsl (below sea level). Resistivities between 1–100 ohm-m are required and the preferred value is 10 ohm-m. Resistivity values as high as 1000 ohm-m beneath site 105 are permissible in the small region above Moho (unnumbered box in Figure 3b) as long as there are average values of less than 100 ohm-m in the mantle from depths of 30–70 km bsl [*Park and Bielinski*, 1999]. However, this region also has anomalously low shear wave velocity [*Jones and Phinney*, 1999].

[27] The block of generally resistive upper crust between sites 105 and 118, which includes the active Panamint Valley fault zone (Figure 3b), is disrupted by small-scale but prominent conductors (zones 2, 3 and 4). Average resistivities of less than 10 ohm-m are preferred in all three zones. Of these three, only zone 3, which corresponds to the active fault zone, appears to extend to depth, although it does not appear to be as conductive at depth as those corresponding to active structures in Owens Valley and Death Valley. The complicated pattern of a resistive body surrounded by conductive regions in zone 4 is also required. However, the top of the conductor at depths of ~12–17 km bsl in this zone could be moved upward to a depth of 8 km bsl without altering significantly the fit to the data. The implications of this alternative model will be compared later to the regions of anomalous shear wave velocities reported by *Jones and Phinney* [1999].

[28] The prominent conductor below Death Valley (zone 5) extends from the surface to depths of 20 km bsl, but the extremely low resistivities (<10 ohm-m) are only necessary in the upper 5 km. At the deeper levels, there is a preference for an average resistivity value of less than 100 ohm-m, indicating that a significant anomaly persists downward through most of the crust. The data at site 123 were fit much better with a conductor below 5 km in zone 5 than with a more resistive body. The prominent conductor below ~12 km depth beneath sites 124–129 is the upper extension of a mantle conductor with preferred resistivities of less than 10 ohm-m [*Park and Bielinski*, 1999]. Finally, the resistive knob beneath Death Valley at depths greater than ~35 km is the uppermost, crustal projection of a mantle region that must be more resistive than 100 ohm-m [*Park*, 2002].

[29] The conductor in zone 5 continues eastward beneath sites 124 and 125 at depths of 2–7 km bsl (Figure 3b), extending beneath the crystalline basement of the Black Mountains (Figures 1 and 2). While some conductive rocks are needed in this region, an alternate model (inset in Figure 3b) fits the data as well as the preferred model. This alternate model requires only 1.2 km of rock with resistivities of 5–10 ohm-m at depths of 2.0–3.2 km bsl. As will be discussed later, this alternate model matches the geology much better.

[30] Zones 6 and 7 were tested because they correlate with known sections of carbonate aquifers. These were shallow features, and we determined bounds on the minimum depth to which these features must extend. Average resistivities of 10 ohm-m were found for both zones. The base of zone 6 could be as shallow as 3 km bsl, and zone 7 could have a base at 2 km bsl.

6. Discussion

[31] In comparing the geologic and resistivity sections (Figure 5), the correspondence between the deeply penetrating conductivity anomalies (zones 1, 3 and 5) and active structures implies that the structures extend at least to mid-crustal depths. Zone 1 dips moderately to steeply westward, suggesting that either the Owens Valley fault is not a steeply dipping fault, as might be inferred from its steep surface trace, or that it is truncated at depth by the west dipping fault bounding the western side of the Coso Range. Whichever of these possibilities may be correct, the geometry is not consistent with the concept of a single steeply dipping zone of simple shear controlling the tectonic pattern [e.g., *Savage et al.*, 1990]. In contrast, zones 3 and 5 appear to

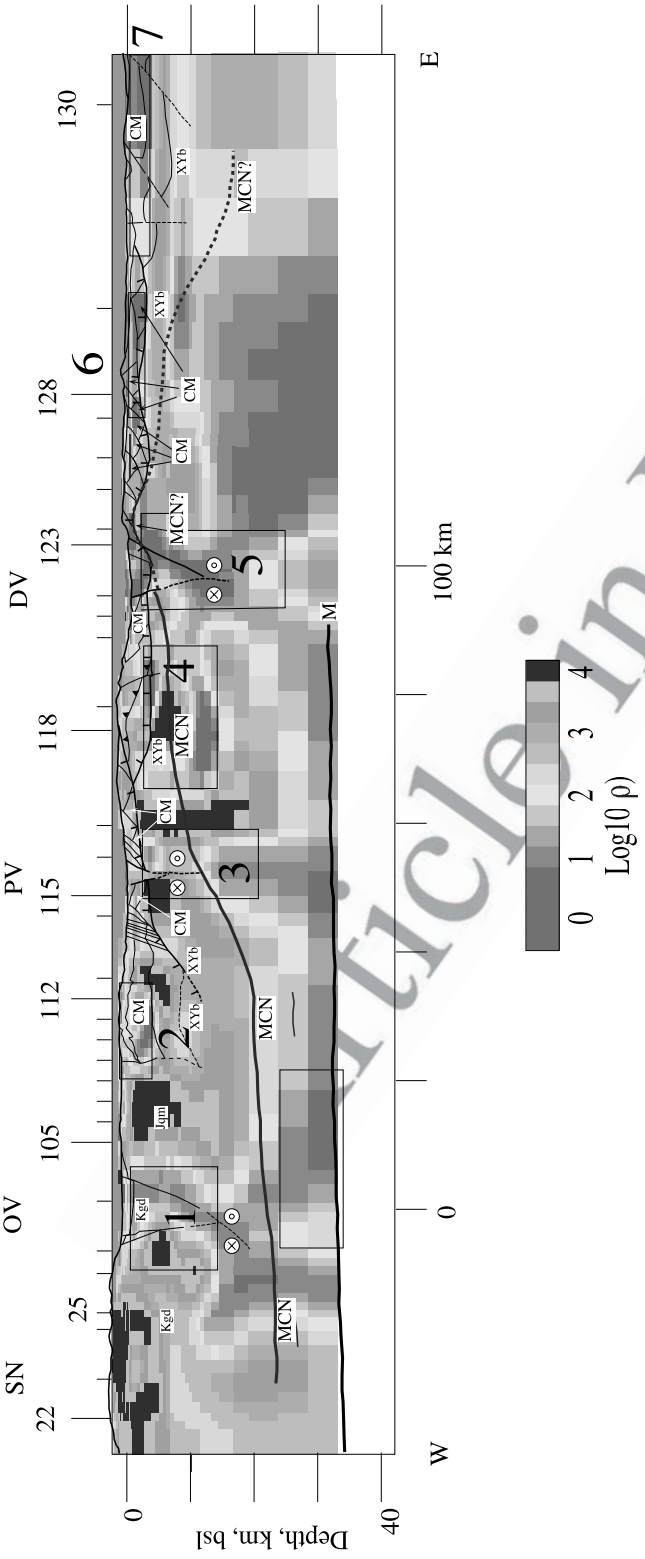

extend nearly vertically through the crust, even though structures at the surface along the line of section have a substantial component of dip-slip displacement. Hence we represent these two classic ''pull apart'' basins as negative flower structures (Figure 3a). Such a representation, which implies strike-slip motion is predominant over dip-slip motion, is independently indicated from geodetic measurements across the region, which are dominated by simple shear [*Bennett et al.*, 1999; *Gan et al.*, 2000].

[32] The extension of the conductor in zone 5 eastward beneath sites 124 and 125 at depths of 2 to 6 km bsl poses an apparent problem because these sites are underlain at shallow depth by crystalline rocks of the Black Mountains (Figure 3a). Based on the geologic constraints, the top of the crystalline basement lies at a depth of no more than about 2 to 3 km bsl, where it is overlain tectonically by late Tertiary sediments of the Furnace Creek basin. Although this conductor in the preferred model falls mostly within crystalline basement, the alternate model discussed above fits the data equally well with a conductive zone restricted to depths of 2.0 to 3.2 km bsl (Figure 3b). As the Furnace Creek basin is a major conduit for regional discharge in the southern Great Basin, a shallow conductive layer with resistivities near 10 ohm-m is reasonable. The apparent problem of having conductive crystalline basement is thus easily explained by water-saturated sediments in the Furnace Creek basin.

[33] Earlier interpretations of teleseismic data in the area revealed the presence of a pronounced velocity inversion (mid-crustal negative, or MCN) associated with strong, east-west anisotropy [*Jones and Phinney*, 1999]. From west to east, the MCN is observed at 22 km bsl beneath site 25 in the easternmost Sierra and at 20 km bsl below site 112 on the Darwin Plateau (Figure 3a). Later work with a seismic array at site 118 in the Panamint Range showed that the MCN was located at a depth of just 6–8 km bsl (R. A. Phinney, oral communication, 2001). Eastward projection of the MCN below sites 112 and 118 would suggest it reaches surficial levels in the Black Mountains (longitude of site 124), where a downward transition from underformed Miocene and Proterozoic crystalline rocks to Tertiary mylonites is exposed.

[34] The MCN, if regarded as the upper boundary to a zone of lateral crustal flow, would be laterally continuous beneath our MT profile if still active. An accumulation of fluids at the top of the MCN would explain the low shear wave velocities, and predict high conductivities. The MCN beneath site 112 corresponds to a transition from shallower

Figure 5. (opposite) Comparison of MT section with alternate model from Figure 3 to geologic section. Simplified version of geologic cross-section (Figure 3a) is overlain on the preferred model from Figure 3b. Where it is a detachment fault, the boundary between XYb and the overlying sediments is indicated with a thicker line with single tick marks. See captions for Figures 2 and 3 for explanation of symbols. Note the correspondence between conductive zones in the upper crust and the carbonate aquifers (CM). See color version of this figure at back of this issue.

resistive rocks overlying deeper conductive ones (Figure 5). Although the MCN beneath site 118 falls within the resistive body in zone 4 (Figure 5), sensitivity tests show that the top of the conductor in zone 4 can be moved upward to match the top of the MCN. The MCN beneath site 25, however, does not correspond to such a transition, but any subhorizontal structure here would presumably be overprinted by the Owens Valley fault zone. Thus, of the three sites where the MCN is imaged seismically, the two eastern ones correspond to a downward transition to higher conductivity, but there is no lateral continuity between these transitions (Figure 5). For example, beneath sites 117 and 121, these anomalies are interrupted by resistive bodies. At the one area in which the top of the deep crustal flow channel is exposed in the Black Mountains (near site 124), the upper crust again requires a low resistivity layer (both preferred and alternate models in Figure 3b) but this layer is more likely associated with a shallow sedimentary basin as discussed in the previous paragraph.

[35] In sum, there is no evidence of laterally continuous, subhorizontal layering in the resistivity section associated with the shear zone (Figure 5). Prominent vertical conductivity anomalies dominate the section, and through-going subhorizontal conductors that correspond to previously proposed zones of deep crustal flow are absent. This observation accords with the interpretation that extensional deformation in the region, including the rise of deep crustal rocks in metamorphic core complexes, occurred in the Miocene [e.g., *Holm and Dokka*, 1993; *Snow and Wernicke*, 2000], and contrasts with the present-day regime which is dominated by strike-slip motion.

[36] The lack of correspondence of zones 2, 4, 6, and 7 with active structures, magmatic centers, or thick basin fill, is enigmatic. In the absence of magma, basin brines, or fault-controlled fluid circulation, upper crustal anomalies of this magnitude are rarely observed. Where observed in tectonically stable regions, they are most commonly associated with graphitic films [e.g., *Mareschal et al.*, 1995]. The only likely occurrence of graphite in upper crustal rocks of the region would be in upper Precambrian schists such as those exposed in the Panamint Range. Detailed petrology of these units indicates that while present in some calcic schists, graphite is not common in these metamorphic rocks [e.g., *Labotka*, 1981]. Additionally, resistivities of the carbonate rocks have always been high where measured [*Park and Torres-Verdin*, 1988; *Biehler and MIT 1981 Field Geophysics Camp*, 1987; numerous unpublished ground water studies]. While we cannot exclude the possibility that some graphite may be present, we conclude that it would be very uncommon.

[37] Another possible explanation is that the anomalies represent aquifers. The hydrological system in the region has generally been characterized by an arrangement of aquitards and aquifers defined by the structural disposition of clastic and carbonate strata, respectively, of the Cordilleran miogeocline [*Winograd and Thordarson*, 1968, 1975]. In particular, at the eastern end of the MT profile, a major south directed interbasinal flow system moves through the carbonate section, and includes the Ash Meadows and Furnace Creek regional discharge zones [*Winograd*, 1971]. The very high conductivities of zones 6 and 7, which are just south of Ash Meadows in the southern Amargosa Desert (Figure 2), are best explained as the result of the hydrologically transmissive carbonate aquifer at depth. This is corroborated by the observation that in the adjacent Black Mountains, which comprises impermeable crystalline and siliciclastic rocks, no such electrical anomaly is observed except as discussed above in relation to the Tertiary strata of the Furnace Creek basin.

[38] We interpret the anomaly in the upper right-hand portion of zone 4 as a aquifer in Neoproterozoic carbonate rocks (below the Paleozoic carbonate aquifer), ponded where they are faulted over impermeable basement rocks at ~2–3 km bsl. Similarly, zone 2 is inferred to be an aquifer ponded along the west dipping base of the Paleozoic carbonate aquifer at ~4–5 km depth beneath the Darwin Plateau, entrapped on the west by the impermeable margin of the batholith.

[39] Although there is a spatial correspondence between zones 2, 4, 6, and 7 and the carbonate units (Figure 5), can the low resistivities be explained reasonably by fluids in the aquifers? Hydrogeochemical analyses of the formation waters in the carbonate aquifers reveal a narrow range of 13–16 ohm-m for the fluid resistivities from springs in the Ash Meadows discharge zone [*Winograd and Thordarson*, 1975]. From additional geochemical analyses of water sampled in boreholes near Ash Meadows [*Claassen*, 1985], we calculated a water resistivity of 9.4 ohm-m and therefore conclude that 10 ohm-m is a reasonable average resistivity for zones 2, 4, 6, and 7. Models relating fluid resistivity and rock resistivity have the form:

$$\rho_{\text{rock}} = \rho_{\text{fluid}} \phi^{-n}, \quad (1)$$

where φ is fractional porosity and n ranges between 1–3 [e.g., *Archie*, 1942]. The exponent (n) accounts for the tortuosity of the current path in the rock. Only a porosity of 100% (i.e., no rock present) can satisfy both a preferred average resistivity of 10 ohm-m and an average fluid resistivity of 10 ohm-m and is therefore unrealistic.

[40] The carbonate aquifers are characterized by low primary porosity in the matrix, but macroscopic secondary porosity due to fracturing as well as dissolution and dolomitization. This secondary porosity contributes to the high permeability (up to 4.4 darcies) and therefore interconnected porosity of the carbonate aquifers [*Winograd and Thordarson*, 1975]. Permeabilities in the aquifers are up to 900,000 times larger than those for the aquitards. While interconnected porosity has not been measured in these carbonates, a study of similar Paleozoic carbonates in the Upper Knox group in the Appalachian region has revealed considerable hydrologic heterogeneity and porosities ranging up to 7.8% [*Montanez*, 1997]. Carbonate cycles of the Upper Knox group have permeabilities in transgressive sequences of up to 1.030 darcies and values of up to 0.14 millidarcies in regressive sequences, indicating considerable heterogeneity within the carbonates. Fluids in the carbonate units of the Cordilleran miogeosyncline in Alberta with total

dissolved solids of 20,000–300,000 ppm and calculated resistivities of ~0.03 ohm-m are found at deeper levels [*Rostron et al.*, 1997]. We therefore conclude that it is possible that fluid resistivities at depths greater than those sampled by *Winograd and Thordarson* [1975] could be much lower and these fluids could be isolated from the shallower levels by aquitards in the carbonates themselves.

[41] If we assume that our preferred value of 10 ohm-m for the zones is correct, then we can calculate the fluid resistivity needed to match this observation. The exponent for fracture networks is approximately 1 [*Waff*, 1974] and for a porosity of 10%, equation (1) yields a fluid resistivity of 1 ohm-m. While 1 ohm-m is lower than that measured by *Winograd and Thordarson* [1975], it is much larger than values seen elsewhere in carbonate aquifers [*Rostron et al.*, 1997] and is therefore reasonable. This estimate of 1 ohm-m assumes that the entire carbonate aquifer is saturated with a fluid of uniform resistivity—an assumption that conflicts with the analyzed samples from *Winograd and Thordarson* [1975]. We therefore suggest that the carbonate aquifers in zones 2, 4, 6, and 7 are saturated with relatively fresh (10 ohm-m) water at shallow levels and with higher density brines (<1 ohm-m) at greater depths. Simple calculations of two horizontal layers acting as parallel conductors show that ~90% of the aquifer can be saturated with relatively fresh water (ρ_w = 10 ohm-m) if the remaining 10% is saturated with a conductive brine (ρ_w = 0.1 ohm-m). This value for the brine, while much more conductive than the shallower waters, is still within a reasonable range compared to observations elsewhere in similar carbonate units [*Rostron et al.*, 1997].

7. Conclusions

[42] Our salient result is that the resistivity image derived for the crust from MT data is dominated by vertical conductors that correspond to active strike-slip faults in the Owens Valley, Panamint Valley, and Death Valley, consistent with geodetic data indicating that contemporary deformation in the region is predominantly strike-slip. Away from the active faults, some zones of low shear wave velocity correspond to subhorizontal conductive zones. These conductive zones are interrupted by subvertical resistive zones, and therefore could not reflect an active system of lateral crustal flow. Where the velocity anomaly occurs beneath an active structure, no subhorizontal conductive zone is observed. The present-day strike-slip tectonic regime apparently produces only vertical structures to depths of ~20 km in the crust and no subhorizontal layers indicative of flow. We infer from the absence of such layers in our electrical section that the tectonic regime in the Miocene, which did generate subhorizontal shear zones, was different from the present-day setting. This conclusion is consistent with observations of laterally continuous layers of anomalously high conductivity in regions of active extension such as the eastern Basin and Range and Rio Grande rift. The discontinuous subhorizontal conductor at ~20 km depth is probably a relict of the Miocene extension.

[43] A surprising result from this study is that the nearly vertical Owens Valley fault zone, located on the west side of Owens Valley, is truncated at a depth of ~8 km bsl by a more prominent, unnamed west dipping fault that bounds the eastern side of Owens Valley. This moderately to steeply dipping fault extends through the middle crust and suggests a local tectonic regime that is more complicated than simple shear along the Owens Valley fault zone and its equivalents.

[44] Several shallower conductive bodies do not correlate with known active structures but instead match the positions of carbonate aquifers known from geological and hydrological data in the region. Given constraints on the geochemistry (and therefore resistivities) of waters from springs and bore holes penetrating these carbonate aquifers, a model of saturation by a fluid of uniform resistivity with depth, as inferred from past hydrologic studies, is precluded. Our results are consistent with fluid compositions measured in these studies only if the aquifer is vertically heterogeneous, with shallow portions saturated with relatively fresh water and deeper levels with more saline brines. A factor of 100 increase in total dissolved solids for brines in the lowermost 10% of the carbonate aquifers would be sufficient to match both the fluid geochemistry and resistivities.

Appendix A

[45] Here we describe, from east to west the data sources and assumptions made in extrapolating surface geology to depth on the cross section in Figure 2, sequentially from east to west. The section was drawn at 1:250,000 using California State Map 2° sheets in California, and a reduced version of the 1:62,500 map of *Burchfiel et al.* [1982] in Nevada, with interpretations based on more detailed maps ranging from 1:24000 to 1:62500. The section is not "balanced," because significant motion normal to the plane of the section has occurred along many of the faults.

[46] Subsurface projection of the Grapevine fault is not well constrained, and thus is shown to dip 45°. *Burchfiel et al.* [1982] reported a vertical component of offset of at least 3.5 km about 10 km north of the section. The geometry of the Montgomery thrust and environs is based on a northward projection of section A–A′ of *Burchfiel et al.* [1982], with the position and offset on the basement nonconformity constrained by post-Pahrump stratigraphic thicknesses provided on their Figure 3. Basement units at depth could in part be Pahrump strata.

[47] The geometry and offset on the Stewart Valley fault is based on northward projection of the trace inferred by *Burchfiel et al.* [1982] and *Schweickert and Lahren* [1997]. Vertical offset of 1.5 km is arbitrary. Growth geometry of lower, middle and upper Miocene units in the Amargosa Desert and Funeral Mountains areas are based on stratigraphic data and synthesis of *Niemi et al.* [2001], which indicate steep dips of lower and middle Miocene strata in the area, versus the relatively gentle folding of upper Miocene strata in the southern Amargosa Desert documented by *Burchfiel et al.* [1982].

[48] Projection of the middle Miocene "breakaway" normal fault beneath the Amargosa Desert is based on northward extrapolation of section C–C′ of *Burchfiel et al.* [1982]. Structural style is probably accurate but exact

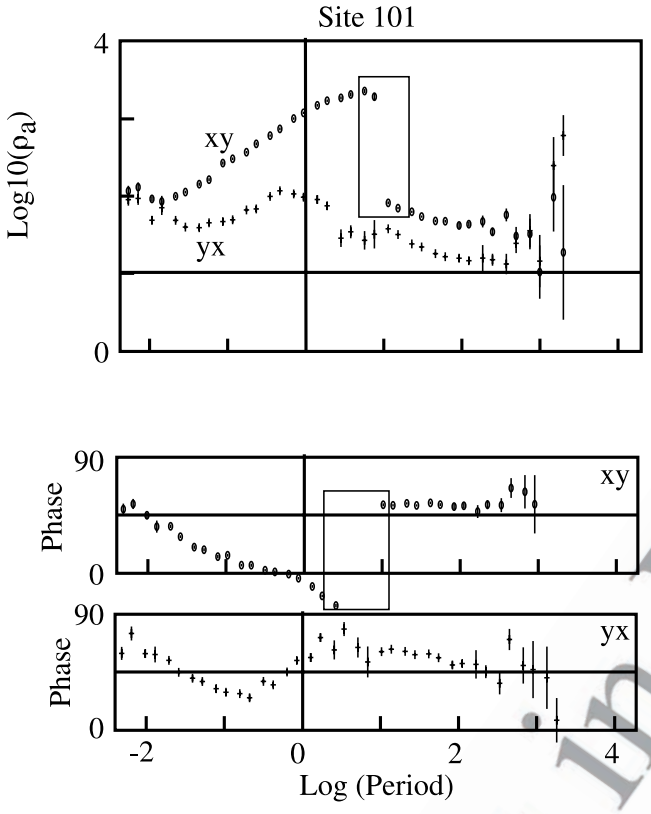

Figure A1. Apparent resistivities and phases for site 101 showing offset in these values at the break between high and low recording bands. With an impedance strike of 0°, the xy mode (circles) is oriented N-S and the yx mode (crosses) is E-W. Error bars for data points are shown as vertical lines. Note the offset in both amplitude and phase at a period of ~10 s in the xy mode (in boxes). This offset was most noticeable at site 101 but was present at all sites in the same recording segment (101–115).

positions of formational contacts and the lower fault of the first tilt block are inferred. The second and third major blocks are exposed in the southeastern Funeral Mountains, with geometries derived mainly from *McAllister* [1971].

[49] Relations in Tertiary and pre-Tertiary strata in the Black Mountains is based on maps of *McAllister* [1970, 1973] and *Holm* [1992], and on discussions summarizing the Furnace Creek basin given by *Snow and Wernicke* [2000] and *Niemi et al.* [2001]. The position of the active trace of the central Death Valley fault zone is based on Plate 3 of *Brogan et al.* [1991]. The depth of Tertiary mylonite is based on projecting 15°N plunge of Badwater "turtleback" antiform onto the section [*Miller*, 1991]. Truncation of turtleback detachment by the central Death Valley fault zone, and the steep dip of the range-front fault is based on *Miller* [1991]. The geometry of faults at depth beneath Death Valley is not well constrained, but may involve a complex interaction among low- and high-angle Quaternary faults, as generally observed along the Black Mountains range front, in the context of a broad negative flower structure. The 3000 m depth of basin fill is based on estimate of *Hunt and Mabey* [1966].

[50] Geometries of normal faults in the Panamint Range are based on the 1:96000 map of *Hunt and Mabey* [1966] and detailed maps and cross sections of *McKenna and Hodges* [1990] and *Hodges et al.* [1990]. The geometry of the Panamint thrust fault at depth beneath the Panamints is extrapolated 20 km southward from relations shown on 1:24000 mapping of the Tucki Mountain area [*Wernicke et al.*, 1993].

[51] The geometry of the shallowly dipping Emigrant fault zone and related splays imbricating upper Miocene/Pliocene hanging wall strata are derived from 1:48000 mapping of *Hall* [1971] and cross sections of *Hodges et al.* [1989].

[52] The geometry of the subsurface projection of the Panamint Valley fault zone is based on re-interpretation of data presented by *Burchfiel et al.* [1987]. They favored downward projection as a very shallow subsurface detachment within a few 100 m of the present valley bottom, based on geophysical and shallow borehole data. These data showed that upper Miocene/Pliocene basalts present in surrounding highlands are not found in the shallow subsur-

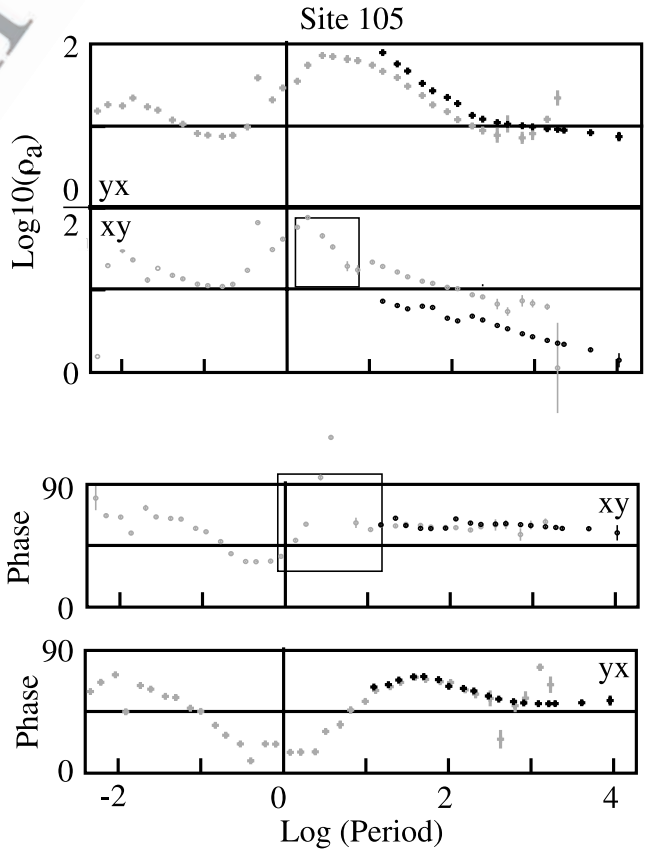

Figure A2. Comparison of broadband and long period data at site 105. xy mode (circles) and yx mode (crosses) are oriented the same as in Figure A1. Grey points are from the broadband instrument and black ones are from the long period one. Note steep decrease in apparent resistivity by ~0.8 decade (in box) and attendant phase associated with shift at recording band boundary.

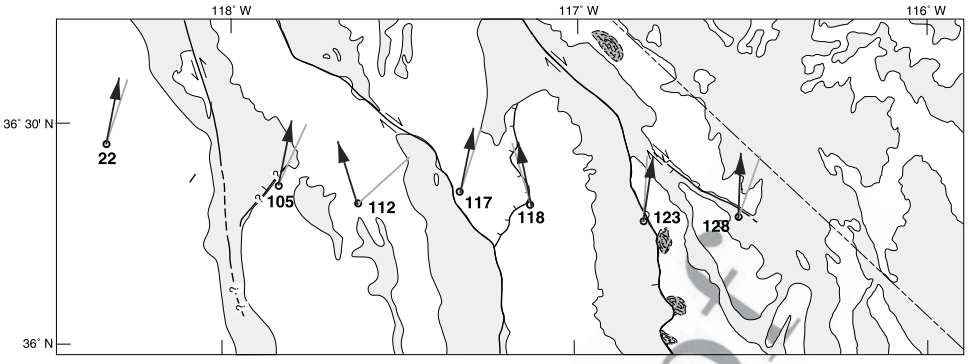

Figure A3. Impedance rotation angles at 100 s periods from long period sites. Note the average N-S strike on these directions. Comparison of the Swift rotation angles (gray lines) and regional strike from the Groom Bailey distortion analysis (black arrows) shows little difference except at site 112. Base map is modified from Figure 2.

face of the basin, which is filled with only a few hundred meters of sediment before Paleozoic is encountered, and so they reasoned that the basalts were tectonically denuded from their Paleozoic substrate along a shallow detachment. We show the basalts projecting to depth and interfingering with a thick section of upper Miocene/Pliocene strata dominated by landslide debris, such as that exposed just north of the line of section at Lake Hill. We show the active fault trace steepening downward into a negative flower structure, and the Tertiary/pre-Tertiary contact at significant depth beneath the valley.

[53] The geology of the Darwin Plateau area is based mainly on 1:48000 map of *Hall and MacKevett* [1962] and on 1:31250 sections G–G′, H–H′ and I–I′ of *Stone et al.* [1989]. Position of the lower part of the miogeosynclinal section extrapolated using stratigraphic thicknesses of *Burchfiel et al.* [1982], which although far to the east appear to be in about the same position within the miogeosynclinal wedge.

[54] The west dipping fault along east margin of Owens Valley is based on the interpretation of a piedmont scarp (discussed in text) by *Streitz and Stinson* [1974]. Position of Owens Valley fault is based on traces mapped by *Beanland and Clark* [1994].

[55] Positions of intrusive contacts in the Sierra Nevada are based on 1:62500 maps of *du Bray and Moore* [1985] and *Moore and Sisson* [1985]. Vertical downward extrapolation of these contacts is based on generally steep exposed margins of plutons and contacts with metasedimentary screens.

Appendix B

[56] The MT soundings were acquired at two different times by two different sets of instruments. The first survey, over 60 broadband (0.008–1024 s) MT soundings from the Great Valley to Death Valley near latitude 36°20′N, was collected by a contractor (Zephyr Geophysical Services) in four segments as part of a larger study of the Sierra Nevada; we use only the easternmost 33 stations for this investigation. Time series were recorded simultaneously at pairs of sites in order to use remote referencing for noise reduction in the analysis. The broadband data were processed by the contractor using remote reference analysis to yield generally reliable impedance estimates over a limited period range of 0.01–200 s. Vertical magnetic fields were measured with surface loops, but the data were very noisy and mostly

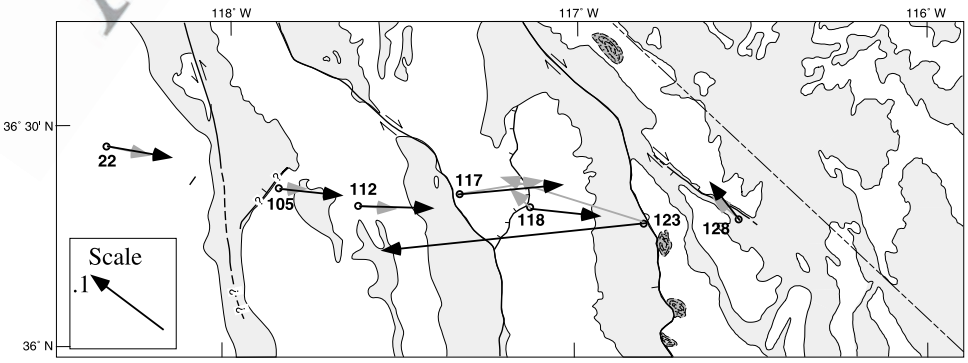

Figure A4. Schmucker induction vectors from the long period sites show a predominant E-W orientation, consistent with a N-S geoelectric strike. Induction vectors are generally small (<0.2) and show little variation from a period of 30 s (gray arrows) to 100 s (black arrows). Note that these are comparable to *Schmuker*'s [1970] induction vectors in Owens Valley at a period of 1800 s.

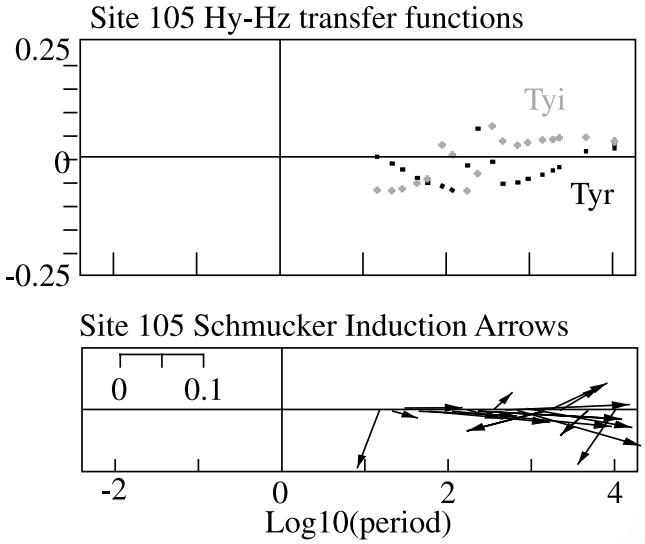

Figure A5. Magnetic transfer functions from site 105 at long periods. Only the Hz-Hy transfer function is shown; the Hz-Hx component is much smaller, as indicated by the E-W orientation of the induction vectors. While there are occasional outliers, most of the induction vectors remain oriented E-W over the range of periods.

unusable. An additional problem was that the N-S impedance estimate (xy) at sites 101–115 had offsets in both apparent resistivity and phase at the boundary between two recording bands (Figure A1), presumably due to faulty instrument calibration. Data within frequency bands were internally consistent, but not between bands. This offset was worst at 101 but present at all sites recorded during a single segment (sites 101–115). We were unable to identify a definitive cause for these offsets (and therefore a correction), and chose instead to give these data lesser weights in the interpretation.

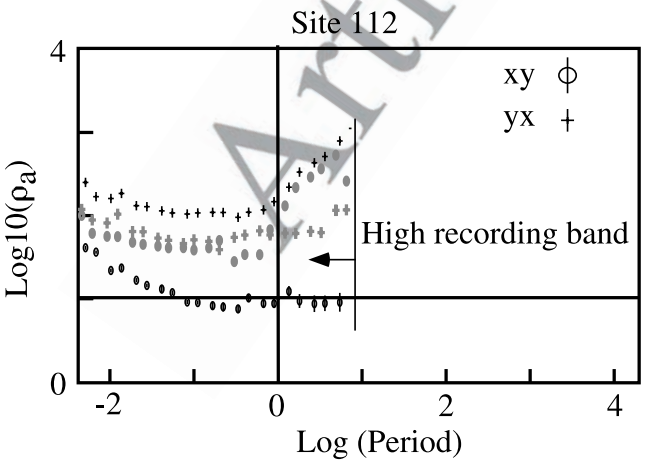

Figure A6. Comparison of apparent resistivities and phases from the high recording band to those from the distortion-corrected tensors at site 112. Modes are labeled as in Figure A1. Data from uncorrected tensors are shown in black and in gray for the distortion-corrected tensors. Note how the anisotropy at short periods (i.e., the separation between the xy and yx apparent resistivities) is reduced by removal of the distortion.

Table A1. Groom-Bailey Distortion Parameters[a]

Site	Regional Azimuth	Twist	Shear
22	−10–10	−20–−10	22–24
23	−10–10	3–13	5–15
24	−10–10	0–15	5–20
25	−1–1	−5–10	15–30
101	−10–10	0	0
102	−10–10	−8–−2	19–25
103	−10–10	0–30	−30–0
105	−10–10	0–10	−5–20
106	−10–10	−10–10	−23–−17
107	−10–10	4–10	−33–−27
108	−10–10	0–10	−30–−20
109	−10–10	−15–1	10–20
110	−2–12	−18–−12	34–40
111	−10–10	−22–−18	−3–2
112	−25–−15	−2–2	−39–−35
113	−15–−5	−27–−23	−7–−3
114	−10–10	−9–−5	−9–−5
115	−10–10	−24–−20	−24–−20
116	0–20	0–6	4–10
117	0–20	2–12	−8–2
118	−10–10	−3–3	−3–3
119	−35–−25	2–12	−8–2
120	25–35	−7–−3	−12–−8
121	0–20	5–9	−2–2
122	−10–10	−2–2	−17–−13
123	−10–10	−5–5	−10–0
124	−5–5	−20–−10	10–20
125	−5–5	0–10	0–10
126	0–20	−15–1	−15–1
127	−10–10	−10–10	−10–10
128	−10–10	0	0
129	−10–10	−10–10	−10–10
130	0	−5	−5

[a]All angles are in degrees and azimuths referenced to north. Sites in bold have both broadband and long period data.

[57] Because of the questionable broadband data quality at longer periods, we reoccupied 7 sites in 1997 with long period MT instruments (Long period Intelligent Magnetotelluric Systems–LIMS) loaned to us by the University of Washington. Data were recorded for periods of up to one month per site. The time series for these sites were analyzed for impedance tensors and magnetic transfer functions using robust processing [*Chave et al.*, 1987]. When the long period impedances are compared to the broadband ones, the former are clearly smoother and less noisy at periods longer than 100 s (Figure A2).

[58] The crustal section presented here is derived from a composite data set formed from merging the broadband and long period impedances and magnetic transfer functions. The goal of the merger was to produce smooth transfer functions across the transition between the two data sets. Because the long period sites were acquired 4 years after the broadband ones, relocating the exact sites (including electrode and coil holes) was impossible. Instead, we installed the long period sites at the latitudes and longitudes given for the broadband sites. Small positional uncertainties lead to slight offsets in the apparent resistivities (Figure A2). We

t2.1 **Table A2.** Static Shift Parameters[a]

t2.2 Site	xy Shift	yx Shift	Criteria
t2.3 102	0.61	1.33	geometric mean of site
t2.4 106	2.09	1	matches 105 xy,yx
t2.5 107	0.80	1.31	matches 105 xy,yx
t2.6 110	0.07	1	matches 109 xy,yx
t2.7 111	0.33	1	matches 112
t2.8 **112**	1	0.73	matches 111
t2.9 113	0.83	1.03	geometric mean of site
t2.10 116	1.51	0.78	geometric mean of 116,117
t2.11 **117**	1.16	0.64	geometric mean of 116,117
t2.12 121	0.89	1.13	geometric mean of site
t2.13 124	0.83	1	geometric mean of 123,124xy
t2.14 126	0.80	0.93	geometric mean of 126,127
t2.15 127	1.09	1.19	geometric mean of 126,127

t2.16 [a] Only sites with nonunity multiplicative factors are listed.

Table A3. Long Period-Broadband Shift Factors t3.1

Site	xy Shift	yx Shift	
022	1.125	4.763	t3.3
105	1.764	0.708	t3.4
112	1.639	0.902	t3.5
117	1.093	1.000	t3.6
118	1.000	1.210	t3.7
123	1.561	1.685	t3.8
128	2.170	1.624	t3.9

used four steps to correct this offset and merge the data sets: identify regional geoelectrical strike; rotate impedance tensors and magnetic transfer functions to regional strike; shift long period apparent resistivities for principal modes to those of broadband data; and splice shorter periods of broadband data onto longer period data.

[59] We estimated geoelectrical strike with a variety of methods. First, we found that strikes from standard tensor rotations [*Swift*, 1967] are somewhat variable but aligned subparallel to the overall regional geologic strike of N10W (Figure A3). While the local geologic map shows a more northwesterly strike in this region (Figure 2), this is an artifact of offset, N-S basins above and below the profile. Next, induction vectors are aligned generally in an E-W direction (Figure A4; induction vectors). Induction vectors, typically aligned perpendicular to geoelectric strike in a 2-D structure [*Schmucker*, 1970], are therefore consistent with the geological and impedance strikes. Last, induction vectors were generally consistent over the longer periods (Figure A5). We therefore chose a geoelectrical strike of 0°, thereby orienting the xy mode N-S and the yx mode E-W. Note that the magnetic transfer functions were also rotated to this regional strike.

[60] Impedance transfer functions often exhibit distortions due to local heterogeneities, and there are several schemes to estimate and remove these effects [e.g, *Groom and Bailey*, 1989; *Chave and Smith*, 1994]. Several of our sites exhibit distortions, identified by the offset of apparent resistivities at the highest frequencies (Figure A6). We used the method of *Groom and Bailey* [1989] to reduce the distortions. This method assumes that a regional 2-D impedance tensor with constant geoelectrical strike is distorted by a shallow heterogeneity characterized by frequency-independent rotation angles called the twist and shear. Regional 2-D impedances differed little from the principal impedances derived from tensor rotation at most sites (Table A1; twist and shear equal to 0 means no distortion). Because the Groom-Bailey distortion is caused presumably by a shallow heterogeneity, distortion parameters were calculated only from the broadband data. All periods were used at most sites, but only the shorter periods (<10 s) were used at sites 101–115. These data are from one recording band, so the offset (Figure 1) should not have affected the distortion analysis. A few sites were improved significantly; the high frequency anisotropy in apparent resistivities at site 112 was reduced by 80% (Figure A6). Note that the Groom-Bailey distortion analysis cannot remove a residual anisotropy (the "static shift"); these static shifts were calculated for the broadband data using the criteria in Table A2. They were then applied to the observed data prior to inversion.

[61] In the final step, we compared the principal modes of the 2-D regional impedance tensor from the long period and broadband data in order to estimate the shift parameters needed to align the apparent resistivities. These multiplicative shifts were generally close to 1, and the largest was almost 5 (Table A3). The apparent resistivities and phases modeled in Figure A4 are a splice between the long period data and the broadband data, with boundaries between the data sets at 20–100s depending on site. Given the poor quality of the broadband data at longer periods, we concluded that splicing was superior to merging overlapping segments of data.

[62] **Acknowledgments.** Support from the National Science Foundation's Continental Dynamics Programs under grants EAR9526992 (S. K. Park) and EAR9526895 (B. Wernicke) is gratefully appreciated. Broadband data acquisition was supervised by George Jiracek for MT stations 101–130. Robert Bielinski, Scott Elrick, and Richard Funk helped in the data acquisition for the long period stations in 1997. We also thank Death Valley National Park and Sequoia-Kings Canyon National Park scientists for their assistance in this study. Reviews by Phillip Wannamaker, John Booker, and Associate Editor Darrel Cowan helped improve this manuscript greatly.

References

Archie, G. E., The electrical resistivity log as an aid in determining some reservoir characteristics, *Trans. Am. Inst. Min. Metall. Pet. Eng.*, *146*, 54–62, 1942.

Beanland, S., and M. M. Clark, The Owens Valley Fault Zone, Eastern California, and surface faulting associated with the 1872 earthquake, *U.S. Geol. Surv. Bull.*, *B-1982*, 29 pp., 4 sheets, 1994.

Bennett, R. A., J. L. Davis, and B. P. Wernicke, Present-day pattern of Cordilleran deformation in the western United States, *Geology*, *27*, 371–374, 1999.

Bennett, R. A., B. P. Wernicke, N. A. Niemi, A. M. Friedrich, and J. L. Davis, Contemporary strain rates in the northern Basin and Range province from GPS data, *Tectonics*, *22*(2), 1008, doi:10.1029/2001TC001355, 2003.

Biehler, S., and MIT 1985 Field Geophysics Camp, A geophysical investigation of the northern Panamint Valley, Inyo County, California, *J. Geophys. Res.*, *92*, 10,427–10,472, 1987.

Brogan, G. E., K. S. Kellogg, D. B. Slemmons, and C. L. Terhune, Late Quaternary faulting along the Death Valley-Furnace Creek fault system, California and Nevada, *U.S. Geol. Surv. Bull.*, *B-1991*, 23 pp., 4 sheets, 1991.

Burchfiel, B. C., and J. H. Stewart, "Pull-apart" origin for the central segment of Death Valley, Ca-

lifornia, *Geol. Soc. Am. Bull.*, *77*, 439–442, 1966.

Burchfiel, B. C., G. S. Hamill, and D. E. Wilhelms, Stratigraphy of the Montgomery Mountains and the northern half of the Nopah and Resting Spring Ranges, Nevada and California, *Geol. Soc. Am. Map Chart Ser., MC-44*, 9 pp., 2 sheets, 1982.

Burchfiel, B. C., K. V. Hodges, and L. H. Royden, Geology of Panamint Valley-Saline Valley pull-apart system, California: Palinspastic evidence for low-angle geometry of a Neogene range-bounding fault, *J. Geophys. Res.*, *92*, 10,422–10,426, 1987.

Chave, A. D., and J. T. Smith, On electric and magnetic galvanic distortion tensor decompositions, *J. Geophys. Res.*, *99*, 4669–4692, 1994.

Chave, A. D., D. J. Thomson, and M. E. Ander, On the robust estimation of power spectra, coherences, and transfer functions, *J. Geophys. Res.*, *92*, 633–648, 1987.

Claassen, H. C., Sources and mechanisms of recharge for ground water in the west-central Armagosa Desert, Nevada: A geochemical interpretation, *U.S. Geol. Surv. Prof. Pap., 712F*, F1–F31, 1985.

de Groot-Hedlin, C., and S. Constable, Occam's inversion to generate smooth two-dimensional models from magnetotelluric data, *Geophysics*, *55*, 1613–1624, 1990.

du Bray, E. A., and J. G. Moore, Geologic map of the Olancha Quandrangle, Southern Sierra Nevada, California, *U.S. Geol. Surv. Map, MF-1734*, 1 sheet, 1985.

Fliedner, M. M., et al., Three-dimensional crustal structure of the southern Sierra Nevada from seismic fan profiles and gravity modeling, *Geology*, *24*, 367–370, 1996.

Gan, W., J. L. Svarc, J. C. Savage, and W. H. Prescott, Strain accumulation across the Eastern California Shear Zone at latitude 36°30′N, *J. Geophys. Res.*, *105*, 16,229–16,236, 2000.

Groom, R. W., and R. C. Bailey, Decomposition of magnetotelluric impedance tensors in the presence of local three-dimensional galvanic distortion, *J. Geophys. Res.*, *94*, 1913–1925, 1989.

Hall, W. E., Geology of the Panamint Butte Quadrangle, Inyo County, California, *U.S. Geol. Surv. Bull.*, *1299*, 67 pp., 1971.

Hall, W. E., and E. M. MacKevett Jr., Geology and ore deposits of the Darwin Quadrangle Inyo County, California, *U.S. Geol. Surv. Prof. Pap., 368*, 87 pp., 4 sheets, 1962.

Hodges, K. V., L. W. McKenna, J. Stock, J. Knapp, L. Page, K. Sternlof, D. Silverberg, G. Wüst, and J. D. Walker, Evolution of extensional basins and Basin and Range topography west of Death Valley, California, *Tectonics*, *8*, 453–467, 1989.

Hodges, K. V., L. W. McKenna, and M. B. Harding, Structural unroofing of the central Panamint Mountains, Death Valley region, southeastern California, in *Basin and Range Extensional Tectonics Near the Latitude of Las Vegas, Nevada*, edited by B. P. Wernicke, *Mem. Geol. Soc. Am., 176*, 377–390, 1990.

Hoisch, T. D., and C. Simpson, Rise and tilt of metamorphic rocks in the lower plate of a detachment fault in the Funeral Mountains, Death Valley, California, *J. Geophys. Res.*, *98*, 6805–6827, 1993.

Hoisch, T. D., M. T. Heizler, and R. E. Zartman, Timing of detachment faulting in the Bullfrog Hills and Bare Mountain area, southwest Nevada: Inferences from $^{40}Ar/^{39}Ar$, K-Ar, U-Pb, and fission track thermochronology, *J. Geophys. Res.*, *102*, 2815–2833, 1997.

Holm, D. K., Structural, thermal, and paleomagnetic constraints on the tectonic evolution of the Black Mountains crystalline terrane, Death Valley region, California, and implications for extensional tectonism, Ph.D. dissertation, Harvard Univ., Cambridge, Mass., 1992.

Holm, D. K., and R. Dokka, Interpretation and tectonic implications of cooling histories: An example from the Black Mountains, Death Valley extended terrane, California, *Earth Planet. Sci. Lett.*, *116*, 63–80, 1993.

Hunt, C. B., and D. R. Mabey, Stratigraphy and structure Death Valley, California, *U.S. Geol. Surv. Prof. Pap., 494-A*, 162 pp., 4 sheets, 1966.

Jennings, C. W., Geologic map of California, 1:750,000 scale, Calif. Div. of Mines and Geol., Sacramento, 1977.

Jiracek, G. R., W. L. Rodi, and L. L. Vanyan, Implications of magnetotelluric modeling for the deep crustal environment in the Rio Grande rift, *Phys. Earth Planet. Inter.*, *45*, 179–192, 1987.

Jones, A. G., Electrical conductivity of the continental lower crust, in *Continental Lower Crust*, edited by D. M. Fountain, R. J. Arculus, and R. W. Kay, pp. 81–143, Elsevier Sci., New York, 1992.

Jones, C. H., and R. A. Phinney, Seismic structure of the lithosphere from teleseismic converted arrivals observed at small arrays in the southern Sierra Nevada and vicinity, California, *J. Geophys. Res.*, *103*, 10,065–10,090, 1998.

Jones, C. H., and R. A. Phinney, Prospecting for the petrology of the upper mantle: Teleseismic shear waves in the Sierra Nevada, California, *Geol. Soc. Am. Abstr. Programs.*, *31*, A481, 1999.

Labotka, T. C., Petrology of an andalusite-type regional metamorphic terrane, Panamint Mountains, California, *J. Petrol.*, *22*, 261–296, 1981.

Mackie, R. L., T. R. Madden, and S. K. Park, A three-dimensional magnetotelluric investigation of the California Basin and Range, *J. Geophys. Res.*, *101*, 16,221–16,239, 1996.

Mackie, R. L., T. R. Madden, and E. A. Nichols, A magnetotelluric survey of the Loma Prieta earthquake area: Implication for earthquake processes and lower crustal conductivity, in *Loma Prieta, California, Earthquake of October 17, 1989*: *Aftershocks and Postseismic Effects*, edited by P. A. Reasonberg, *U.S. Geol. Surv. Prof. Pap., XX*, D289–D312, 1997.

Mancktelow, N. S., and T. L. Pavlis, Fold-fault relationships in low-angle detachment systems, *Tectonics*, *13*, 668–685, 1994.

Mareschal, M., R. L. Kellett, R. D. Kurtz, J. N. Ludden, and R. C. Bailey, Archean cratonic roots, mantle shear zones, and deep electrical conductivity, *Nature*, *375*, 134–137, 1995.

McAllister, J. F., Geology of the Furnace Creek Borate area, Death Valley, Inyo County, California, *Calif. Div. Mines Geol. Map Sheet, 14*, 9 pp., 1 sheet, 1970.

McAllister, J. F., Preliminary Geologic map of the Amargosa Valley Borate area, Inyo County, California, *U.S. Geol. Surv. Open File Rep.*, *OF71-0186*, 1 sheet, 1971.

McAllister, J. F., Geologic map and sections of the Amargosa Valley Borate area—Southeast continuation of the Furnace Creek area–Inyo County, California, *U.S. Geol. Surv. Misc. Invest. Map, I-782*, 1 sheet, 1973.

McKenna, L. W., and K. V. Hodges, Constraints on the kinematics and timing of late Miocene–Recent extension between the Panamint and Black Mountains, southeastern California, in *Basin and Range Extensional Tectonics Near the Latitude of Las Vegas, Nevada*, edited by B. P. Wernicke, *Mem. Geol. Soc. Am.*, *176*, 363–376, 1990.

Miller, M. G., High-angle origin of the currently low-angle Badwater Turtleback fault, Death Valley, California, *Geology*, *19*, 372–375, 1991.

Montanez, I. P., Secondary porosity and late diagenetic cements of the upper Knox group, central Tennessee region: A temporal and spatial history of fluid flow conduit development within the Knox regional system, in *Basin-Wide Diagenetic Patterns*: *Integrated Petrologic, Geochemical, and Hydrologic Considerations*, edited by I. P. Montanez, J. M. Gregg, and K. L. Shelton, pp. 101–117, Soc. for Sediment. Geol., Tulsa, Okla., 1997.

Moore, J. G., and T. W. Sisson, Geologic Map of the Kern Peak Quadrangle, Tulare County, California, *U.S. Geol. Surv. Map, GQ-1584*, 1 sheet, 1985.

Nabighian, M. N., *Electromagnetic Methods in Applied Geophysics*, Soc. of Explor. Geophys., Tulsa, Okla., 1991.

Niemi, N. A., B. P. Wernicke, R. J. Brady, J. B. Saleeby, and G. C. Dunne, Distribution and provenance of the middle Miocene Eagle Mountain Formation, and implications for regional kinematic analysis of the Basin and Range province, *Geol. Soc. Am. Bull.*, *113*, 419–442, 2001.

Park, S. K., Transformation of electrical resistivity cross sections into temperature and melt fraction sections: A progress report, paper presented at the XVIth Biennial Induction Workshop, Int. Assoc. of Geomagn. and Aeron., Santa Fe, New Mex., 2002.

Park, S. K., and R. Bielinski, Electrical conductivity images of extended crust, Sierra Nevada-Death Valley, California, *Geol. Soc. Am. Abstr. Programs*, *31*, A481, 1999.

Park, S. K., and C. Torres-Verdin, A systematic approach to the interpretation of magnetotelluric data in volcanic environments with applications to the quest for magma in Long Valley, California, *J. Geophys. Res.*, *93*, 13,265–13,283, 1988.

Park, S. K., B. Hirasuna, G. R. Jiracek, and C. L. Kinn, Magnetotelluric evidence of lithospheric mantle thinning beneath the southern Sierra Nevada, *J. Geophys. Res.*, *101*, 16,241–16,255, 1996.

Rodi, W. L., and R. L. Mackie, Nonlinear conjugate gradients algorithm for 2-D magnetotelluric inversion, *Geophysics*, *66*, 174–187, 2001.

Rostron, B. J., J. Toth, and H. G. Machel, Fluid flow, hydrochemistry, and petrological entrapment in Devonian reef complexes, south-central Alberta, Canada, in *Basin-Wide Diagenetic Patterns*: *Integrated Petrologic, Geochemical, and Hydrologic Considerations*, edited by I. P. Montanez, J. M. Gregg, and K. L. Shelton, pp. 139–156, Soc. for Sediment. Geol., Tulsa, Okla., 1997.

Savage, J. C., M. Lisowski, and W. H. Prescott, An apparent shear zone trending north-northwest across the Mojave Desert into Owens Valley, eastern California, *Geophys. Res. Lett.*, *17*, 2113–2116, 1990.

Schmucker, U., Anomalies of geomagnetic variations in the southwest United States, Ph.D. dissertation, Univ. of Calif., San Diego, 1970.

Schweickert, R. A., and M. M. Lahren, Strike-slip fault system in Amargosa Valley and Yucca Mountain, Nevada, *Tectonophysics*, *272*, 25–41, 1997.

Serpa, L., and T. L. Pavlis, Three-dimensional model of the Cenozoic history of the Death Valley region, southeastern California, *Tectonics*, *15*, 1113–1128, 1996.

Smith, J. T., and J. R. Booker, Rapid inversion of two- and three-dimensional magnetotelluric data, *J. Geophys. Res.*, *96*, 3905–3922, 1991.

Snow, J. K., and B. Wernicke, Cenozoic tectonism in the central Basin and Range: Magnitude, rate, and distribution of upper crustal strain, *Am. J. Sci.*, *300*, 659–719, 2000.

Stone, P., G. C. Dunne, C. H. Stevens, and R. M. Gulliver, Geologic map of Paleozoic and Mesozoic rocks in parts of the Darwin and adjacent quadrangles, Inyo County, California, *U.S. Geol. Surv. Map, I-1932*, 2 sheets, 1989.

Streitz, R., and M. C. Stinson, The Geologic map of California, Death Valley Sheet, (scale 1:250,000), Calif. Div. of Mines and Geology, Sacramento, 1974.

Swift, C. M., Jr., A magnetotelluric investigation of an electrical conductivity anomaly in the southwestern United States, Ph.D. dissertation, Mass. Inst. of Technol., Cambridge, 1967.

Tullis, J., R. Yund, and J. Farver, Deformation-enhances fluid distribution in feldspar aggregates and implications for ductile shear zones, *Geology*, *24*, 63–66, 1996.

Unsworth, M. J., P. E. Malin, G. D. Egbert, and J. R. Booker, Internal structure of the San Andreas fault at Parkfield, California, *Geology*, *25*, 359–362, 1997.

Vozoff, K., The magnetotelluric method, in *Electromagnetic Methods in Applied Geophysics*, edited by M. N. Nabighian, pp. 641–711, Soc. of Explor. Geophys., Tulsa, Okla., 1991.

Waff, H. S., Theoretical considerations of electrical conductivity in a partially molten mantle and implications for geothermometry, *J. Geophys. Res.*, *79*, 4003–4010, 1974.

Wannamaker, P. E., Affordable magnetotellurics: Interpretation in natural environments, in *Three-Dimensional Electromagnetics*, *Geophys. Dev. Ser.*, vol. 7, edited by M. Oristaglio and B. Spies, pp. 349–374, Soc. of Explor. Geophys., Tulsa, Okla., 1999.

Wannamaker, P. E., G. W. Hohmann, and S. H. Ward, Magnetotelluric responses of three-dimensional bodies in layered earths, *Geophysics*, *49*, 1517–1533, 1984.

Wannamaker, P. E., J. M. Johnston, J. A. Stodt, and J. R. Booker, Anatomy of the southern Cordilleran hingeline, Utah and Nevada, from deep electric resistivity profiling, *Geophysics*, *62*, 1069–1086, 1997.

Watson, E. B., and A. Lupulescu, Aqueous fluid connectivity and chemical transport in clinopyroxene-rich rocks, *Earth Planet. Sci. Lett.*, *117*, 279–294, 1993.

Wernicke, B., Cenozoic extensional tectonics of the United States Cordillera, in *The Geology of North America*, vol. G3, *The Cordilleran Orogen*: *Conterminous U.S.*, edited by B. C. Burchfiel, P. W. Lipman, and M. L. Zoback, pp. 552–581, Geol. Soc. of Am., Boulder, Colo., 1992.

Wernicke, B., and J. K. Snow, Cenozoic tectonism in the central Basin and Range: Motion of the Sierran-Great Valley Block, *Int. Geol. Rev.*, *40*, 403–410, 1998.

Wernicke, B., G. J. Axen, and J. K. Snow, Basin and range extensional tectonics at the latitude of Las Vegas, Nevada, *Geol. Soc. Am. Bull.*, *100*, 1738–1757, 1988.

Wernicke, B., J. K. Snow, K. V. Hodges, and J. D. Walker, Structural constraints on Neogene Tectonism in the southern Great Basin, in *Crustal Evolution of the Great Basin and Sierra Nevada*, *Cordilleran/Rocky Mountain Section*, *Geol. Soc. Am. Guidebook*, edited by M. M. Lahren, J. H. Trexler Jr., and C. Spinosa, pp. 453–479, Dep. of Geol. Sci., Univ. of Nevada, Reno, 1993.

Wernicke, B., et al., Origin of high mountains in the continents: The southern Sierra Nevada, *Science*, *271*, 190–193, 1996.

Winograd, I. J., Origin of major springs in the Armagosa Desert of Nevada and Death Valley, California, Ph.D. dissertation, Univ. of Ariz., Tucson, Ariz., 1971.

Winograd, I. J., and W. Thordarson, Structural control of ground-water movement in miogeosynclinal rocks of south-central Nevada, in *Nevada Test Site*, edited by E. B. Eckel, *Mem. Geol. Soc. Am.*, *110*, 35–48, 1968.

Winograd, I. J., and W. Thordarson, Hydrogeologic and hydrochemical framework, south-central Great Basin, Nevada-California, with special reference to the Nevada test site, *U.S. Geol. Surv. Prof. Pap. 712C*, 1–126, 1975.

S. K. Park, Institute of Geophysics and Planetary Physics, University of California, Riverside, CA 92521, USA. (magneto@ucrmt.ucr.edu)

B. Wernicke, Division of Geological and Planetary Sciences, California Institute of Technology, Pasadena, CA 91125, USA.

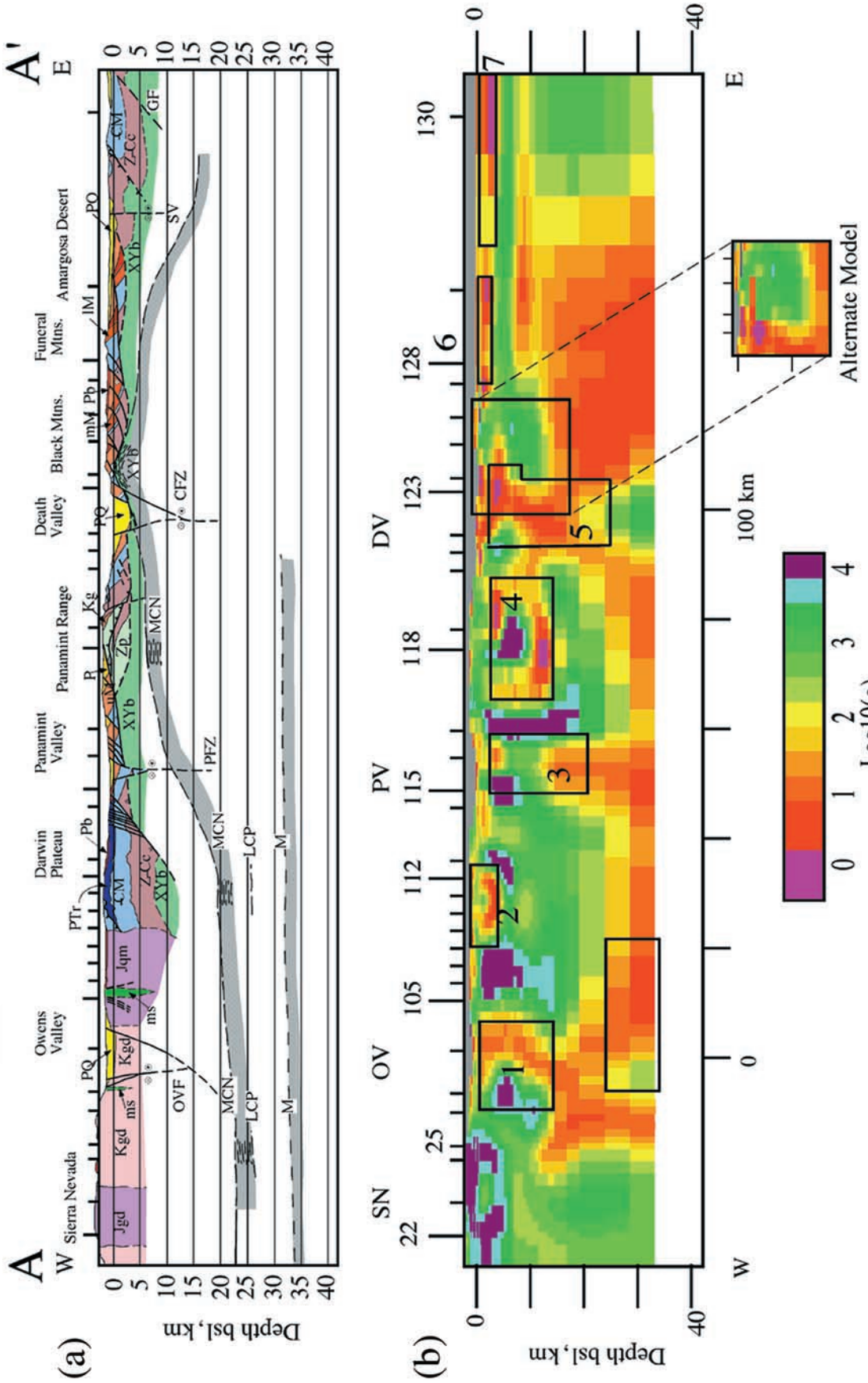
A
A'
W
E
Sierra Nevada
Owens Valley
Darwin Plateau
Panamint Valley
Panamint Range
Death Valley
Black Mtns.
Funeral Mtns.
Amargosa Desert
Jgd
Kgd
ms
Jqm
PTr
PQ
Pb
mM
Kg
Zg
XYb
ZCc
ZM
R
lM
OVF
MCN
LCP
M
PFZ
CFZ
SV
GF
Depth bsl, km
(a)
(b)
SN
OV
PV
DV
W
E
100 km
Alternate Model
Log10(ρ)
1
2
3
4
5
6
7

Figure 3. (opposite) (a) Geologic cross section across MT transect. XYb, Proterozoic crystalline basement; Zp, Pahrump Group; ZCc, Neoproterozoic-Cambrian clastic strata; CM, Cambrian to Mississippian carbonate strata (lower carbonate aquifer), PTr, upper Paleozoic and Triassic strata; ms, metasedimentary screens within Mesozoic plutons; Jqm, Jurassic quartz monzonite; Jgd, Jurassic granodiorite; Kgd, Cretaceous granodiorite; lM, mM and uM, lower, middle and upper Miocene rift basin deposits and intercalated volcanics; P, Pliocene rift deposits; Pb, Pliocene volcanics, mainly basalt; PQ, Pliocene and Quaternary alluvial fill of modern valleys. Dot and cross symbols indicate motion along faults toward and away from reader, respectively. Thrust faults shown with teeth, major detachments with one, two or three tick marks, in order of decreasing age. Tick marks along the top of the section show positions of MT sites. Seismic interfaces from *Jones and Phinney* [1998] shown with heavy dot-dash lines where observed from arrays in the Sierra Nevada, Darwin Plateau and Panamint Range (the latter from R.A. Phinney, oral communication, 2001), interpolations and extrapolations shown with thinner lines and shading. MCN, mid-crustal negative; LCP, lower crustal positive; M, Moho. Fine dashes, Tertiary mylonite zones discussed in text. (b) Preferred MT resistivity cross sections from 2-D inversion. Regions outlined for sensitivity testing (black boxes) are numbered 1–7. See text for results of testing. The MT model is truncated at the base of the crust for comparison to Figure 3a. Inset on MT section shows alternate model for Black Mountains which does not have a thick conductive region east of zone 5. Common logarithm of resistivity is plotted in section; see scale at bottom. This scale is used because of the wide range of values seen in this physical parameter. See captions of Figures 1 and 2 for explanation of symbols.

Figure 4. (opposite) Pseudosections of MT data and associated fits to data from final model. Each section is labeled with the type of data (apparent resistivity or phase) and it orientation (N-S or E-W). Color scales for apparent resistivities and phases are shared, but ranges are labeled differently for these quantities. Similarly, scales for difference pseudosections for apparent resistivity and phase are shared but ranges are different. Sections of data excluded from the inversion are shown with black areas in difference pseudosections. Note that most of the TE mode (i.e., the N-S mode) was not used in the inversion. The difference pseudosections reveal no systematic misfits.

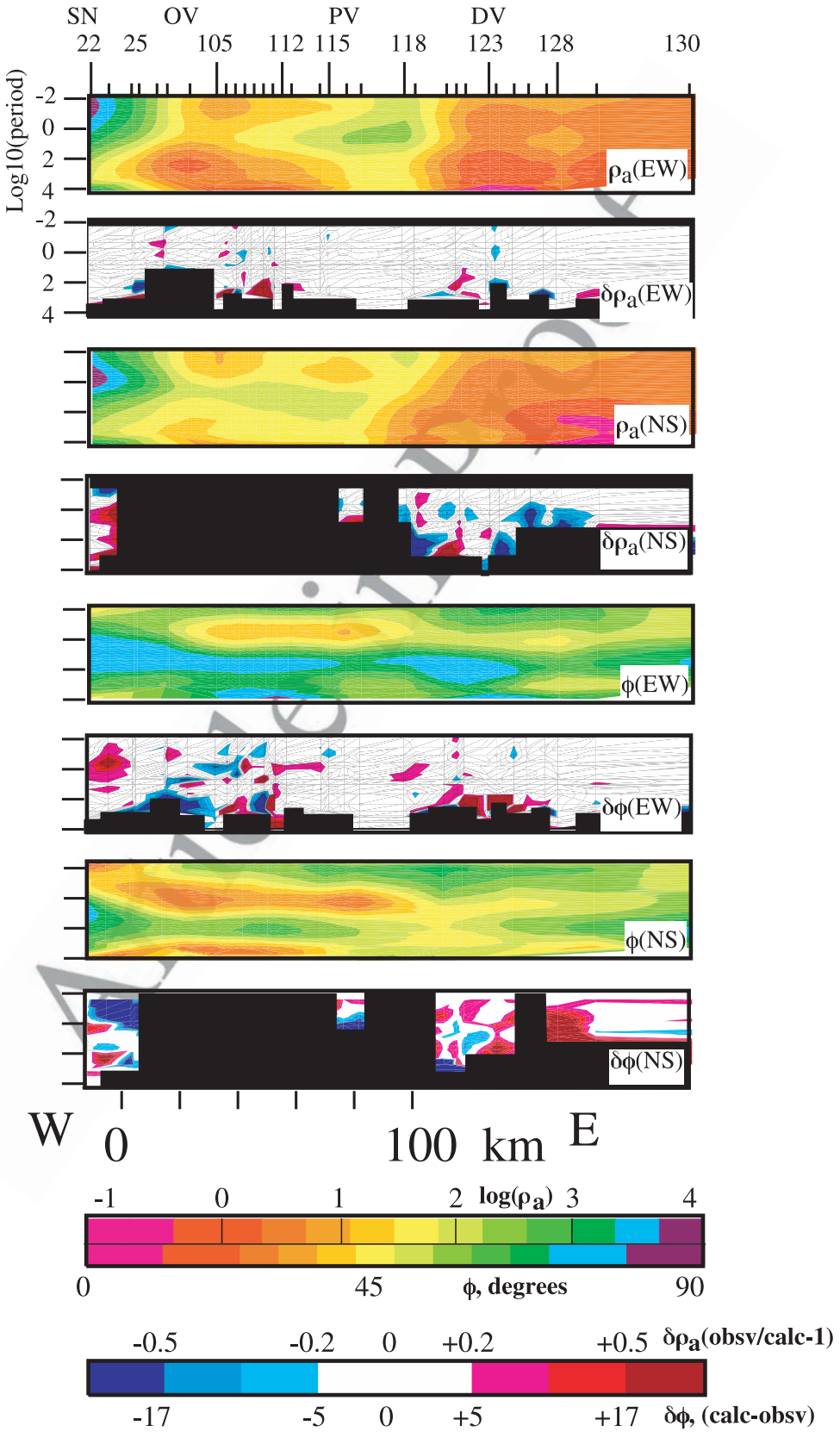
SN
OV
PV
DV
22
25
105
112
115
118
123
128
130
Log10(period)
-2
0
2
4
ρa(EW)
δρa(EW)
ρa(NS)
δρa(NS)
ϕ(EW)
δϕ(EW)
ϕ(NS)
δϕ(NS)
W
0
100 km
E
-1
0
1
2
log(ρa)
3
4
0
45
ϕ, degrees
90
-0.5
-0.2
0
+0.2
+0.5
δρa(obsv/calc-1)
-17
-5
0
+5
+17
δϕ, (calc-obsv)

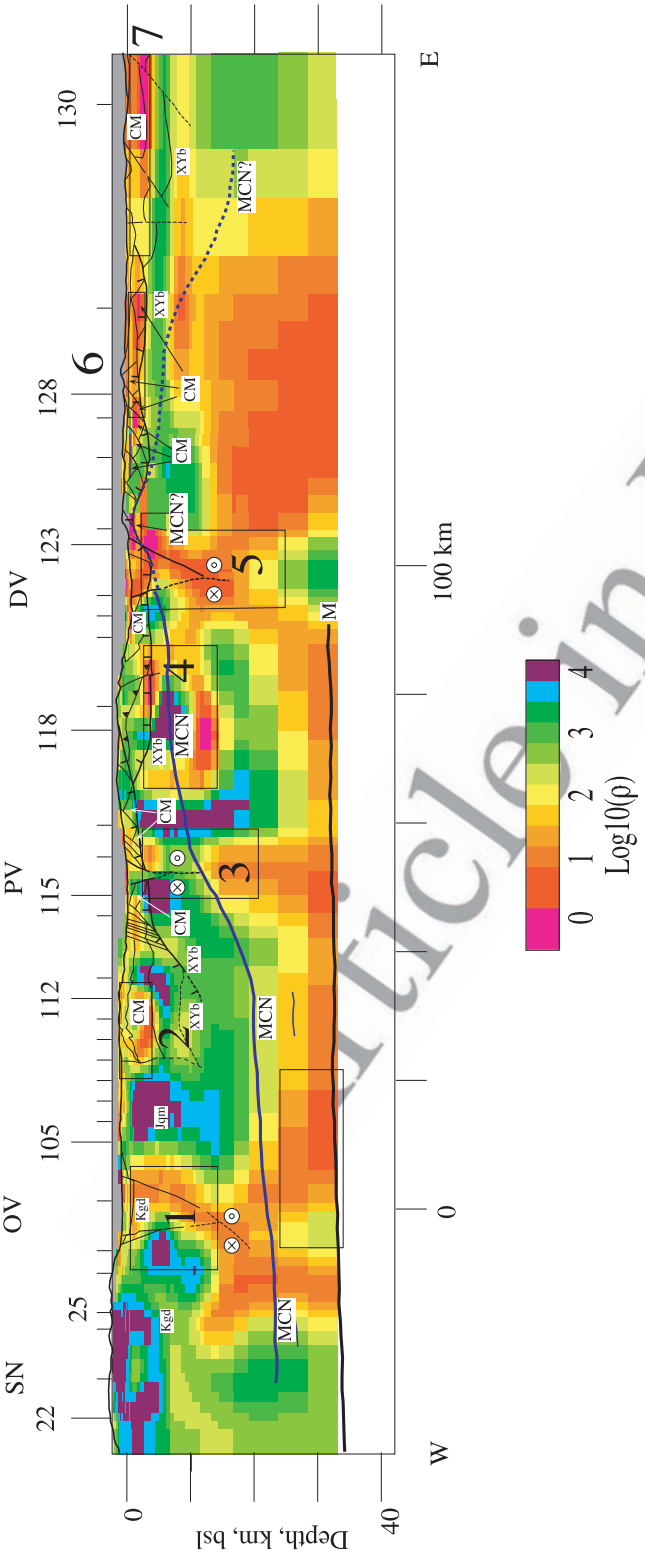

Figure 5. (opposite) Comparison of MT section with alternate model from Figure 3 to geologic section. Simplified version of geologic cross-section (Figure 3a) is overlain on the preferred model from Figure 3b. Where it is a detachment fault, the boundary between XYb and the overlying sediments is indicated with a thicker line with single tick marks. See captions for Figures 2 and 3 for explanation of symbols. Note the correspondence between conductive zones in the upper crust and the carbonate aquifers (CM).